



**Bending of Threaded and Unthreaded Tungsten  
Rods Under Oblique Impact**

**by Martin N. Raftenberg and Todd W. Bjerke**

**ARL-TR-3578**

**August 2005**

## **NOTICES**

### **Disclaimers**

The findings in this report are not to be construed as an official Department of the Army position unless so designated by other authorized documents.

Citation of manufacturer's or trade names does not constitute an official endorsement or approval of the use thereof.

**DESTRUCTION NOTICE**—Destroy this report when it is no longer needed. Do not return it to the originator.

# **Army Research Laboratory**

Aberdeen Proving Ground, MD 21005-5069

---

**ARL-TR-3578**

**August 2005**

---

## **Bending of Threaded and Unthreaded Tungsten Rods Under Oblique Impact**

**by Martin N. Raftenberg and Todd W. Bjerke  
Weapons and Materials Research Directorate, ARL**

# REPORT DOCUMENTATION PAGE

*Form Approved*  
OMB No. 0704-0188

Public reporting burden for this collection of information is estimated to average 1 hour per response, including the time for reviewing instructions, searching existing data sources, gathering and maintaining the data needed, and completing and reviewing the collection information. Send comments regarding this burden estimate or any other aspect of this collection of information, including suggestions for reducing the burden, to Department of Defense, Washington Headquarters Services, Directorate for Information Operations and Reports (0704-0188), 1215 Jefferson Davis Highway, Suite 1204, Arlington, VA 22202-4302. Respondents should be aware that notwithstanding any other provision of law, no person shall be subject to any penalty for failing to comply with a collection of information if it does not display a currently valid OMB control number.

**PLEASE DO NOT RETURN YOUR FORM TO THE ABOVE ADDRESS.**

<b>1. REPORT DATE (DD-MM-YYYY)</b> August 2005		<b>2. REPORT TYPE</b> Final		<b>3. DATES COVERED (From - To)</b> October 2004 to August 2005	
<b>4. TITLE AND SUBTITLE</b>  Bending of Threaded and Unthreaded Tungsten Rods Under Oblique Impact				<b>5a. CONTRACT NUMBER</b>	
				<b>5b. GRANT NUMBER</b>	
				<b>5c. PROGRAM ELEMENT NUMBER</b>	
<b>6. AUTHOR(S)</b>  Martin N. Raftenberg and Todd W. Bjerke (both of ARL)				<b>5d. PROJECT NUMBER</b> 1L162618AH80	
				<b>5e. TASK NUMBER</b>	
				<b>5f. WORK UNIT NUMBER</b>	
<b>7. PERFORMING ORGANIZATION NAME(S) AND ADDRESS(ES)</b> U.S. Army Research Laboratory Weapons and Materials Research Directorate Aberdeen Proving Ground, MD 21005-5069				<b>8. PERFORMING ORGANIZATION REPORT NUMBER</b>  ARL-TR-3578	
<b>9. SPONSORING/MONITORING AGENCY NAME(S) AND ADDRESS(ES)</b>				<b>10. SPONSOR/MONITOR'S ACRONYM(S)</b>	
				<b>11. SPONSOR/MONITOR'S REPORT NUMBER(S)</b>	
<b>12. DISTRIBUTION/AVAILABILITY STATEMENT</b>  Approved for public release; distribution is unlimited.					
<b>13. SUPPLEMENTARY NOTES</b>					
<b>14. ABSTRACT</b>  We employed ballistic experiments and finite element (FE) analysis to explore the extent to which, and the mechanism by which, the threading on a tungsten heavy alloy rod increases its susceptibility to break up under conditions of oblique impact. In the laboratory, small-scale rods with and without threads were launched into thin rolled homogeneous armor plates at 1300 m/s and 60 degrees' obliquity. Fracture near the nose of the rod occurred more consistently with the threaded rods. LS-DYNA <sup>1</sup> was used to analyze plane strain elastic impact of threaded and unthreaded rods striking a rigid surface at 10 m/s and 60 degrees' obliquity. These calculations revealed a greater degree of bending in a threaded rod than in an unthreaded rod of the same diameter. The maximum principal stress, which has been used as a criterion for brittle tensile fracture, also attained larger values in the threaded than in the unthreaded rod. With the aid of static FE analyses of cantilevered, point-loaded, threaded and unthreaded rods, the results of which could be compared with an analytical result from plate theory, we associated the increased bending with a decrease in effective rod thickness.  <sup>1</sup> LS-DYNA, which is not an acronym, is a trademark of Livermore Software Technology Corp.					
<b>15. SUBJECT TERMS</b>  bending; KE rod; oblique impact; threading; tungsten heavy alloy					
<b>16. SECURITY CLASSIFICATION OF:</b>			<b>17. LIMITATION OF ABSTRACT</b>	<b>18. NUMBER OF PAGES</b>	<b>19a. NAME OF RESPONSIBLE PERSON</b>
a. REPORT Unclassified	b. ABSTRACT Unclassified	c. THIS PAGE Unclassified	SAR	50	Martin N. Raftenberg
					<b>19b. TELEPHONE NUMBER (Include area code)</b> 410-306-0949

---

## Contents

---

<b>List of Figures</b>	<b>iv</b>
<b>List of Tables</b>	<b>v</b>
<b>1. Introduction</b>	<b>1</b>
<b>2. Experimental Observations</b>	<b>1</b>
<b>3. Plane-Strain Modeling of Oblique Impact</b>	<b>7</b>
3.1 Problem Definition.....	7
3.2 Meshes.....	9
3.3 WHA Properties.....	9
3.4 Results and Discussion.....	11
3.4.1 Contour Plots of $T_{xx}$ Throughout Rods 7-NT and 7-T.....	11
3.4.2 History Plots of $T_{xx}$ in Rods 7-NT and 7-T at $X = 34.74$ mm.....	12
3.4.3 Profiles of $T_{xx}$ , $T_{yy}$ , $T_{zz}$ , and $T_{xy}$ in Rods 7-NT and 7-T at $X = 34.74$ mm and $t = 32$ $\mu$ s.....	18
3.4.4 Contour Plots of $T_{xx}$ in Rod 7-T in the Vicinity of Threads 1 Through 8.....	20
3.4.5 History Plots of $T_{xx}$ in Rod 7-T at $X = 36.04$ mm.....	20
3.4.6 Profiles of Principal Stresses in Rods 7-NT and 7-T at $X = 35.74$ mm and $t = 32$ $\mu$ s.....	23
<b>4. Conclusions</b>	<b>27</b>
4.1 Summary of Results.....	27
4.2 Assessment.....	28
<b>5. References</b>	<b>29</b>
<b>Appendix A. Flexural Wave Analysis</b>	<b>31</b>
<b>Appendix B. Static Bending of Rods 7-NT and 7-T</b>	<b>35</b>
<b>List of Symbols</b>	<b>41</b>
<b>Distribution List</b>	<b>42</b>

---

## List of Figures

---

Figure 1. Geometry of rod 6A-T.....	2
Figure 2. Geometry of rod 7-T.....	2
Figure 3. Sketch of the experiments; a tungsten rod strikes an RHA plate at 1300 m/s and 60 degrees' obliquity.....	3
Figure 4. Shadowgraphs of rod 6A-T at three times following perforation of an RHA plate; this pattern of separation of a single large nose fragment occurred in all five experiments with 6A-T.....	4
Figure 5. Shadowgraphs of rod 7-T at three times following perforation of an RHA plate; this pattern of separation of a single nose fragment was repeated in four of five experiments with 7-T.....	5
Figure 6. Shadowgraphs of rod 7-T at three times following perforation of an RHA plate from the single experiment in which 7-T fragmented at multiple locations.....	6
Figure 7. A post-perforation shadowgraph of rod 7-NT from each of four experiments; the results show greater experiment-to-experiment variability than with 6A-T and 7-T, and in one experiment, the rod remained intact.....	7
Figure 8. Sketch of the plane-strain problems studied in section 3: a tungsten rod strikes a rigid target at 10 m/s and 60 degrees' obliquity. ....	8
Figure 9. The front portion of rod 7-T, with material and spatial coordinate systems indicated (dimensions are in millimeters).....	8
Figure 10. FE mesh for rod 7-T, (a) overview, (b) front, (c) back, (d) thread.....	10
Figure 11. FE mesh for rod 7-NT, (a) overview, (b) front, (c) back, (d) "top". ....	11
Figure 12. $T_{xx}$ in rod 7-NT at specific times in the range of 5 to 50 $\mu$ s after impact.....	13
Figure 13. $T_{xx}$ in rod 7-NT at specific times in the range of 55 to 100 $\mu$ s after impact.....	14
Figure 14. $T_{xx}$ in rod 7-T at specific times in the range of 5 to 50 $\mu$ s after impact.....	15
Figure 15. $T_{xx}$ in rod 7-T at specific times in the range of 55 to 100 $\mu$ s after impact.....	16
Figure 16. $T_{xx}$ in rod 7-NT along $X = 34.74$ mm as a function of time after impact. (Note the peaks at $t \cong 32 \mu$ s.).....	17
Figure 17. $T_{xx}$ in rod 7-T along $X = 34.74$ mm as a function of time after impact. (Note the peaks at $t \cong 32 \mu$ s.).....	17
Figure 18. Profiles of $T_{xx}$ , $T_{yy}$ , $T_{zz}$ , and $T_{xy}$ in rod 7-NT along $X = 34.74$ mm and at $t = 32 \mu$ s. ...	18
Figure 19. Profiles of $T_{xx}$ , $T_{yy}$ , $T_{zz}$ , and $T_{xy}$ in rod 7-T along $X = 34.74$ mm and at $t = 32 \mu$ s. ....	19
Figure 20. Profiles of $T_{xx}$ in rods 7-NT and 7-T along $X = 34.74$ mm and at $t = 32 \mu$ s. ....	20
Figure 21. $T_{xx}$ in rod 7-T at 20 and 30 $\mu$ s after impact. ....	21
Figure 22. $T_{xx}$ in rod 7-T at 40 and 50 $\mu$ s after impact. ....	22

Figure 23. $T_{xx}$ in rod 7-T along $X = 36.04$ mm as a function of time after impact. (Note the generally small values of $T_{xx}$ at $Y = \pm 5.89$ mm, corresponding to the thread's interior.).....	23
Figure 24. Impact experiment described in Bjerke and Edmanson (2004) and subsequent SEM of fracture surface.....	24
Figure 25. Profiles of principal Cauchy stresses in rod 7-NT along $X = 34.74$ mm and at $t = 32$ $\mu$ s.....	25
Figure 26. Profiles of principal Cauchy stresses in rod 7-T along $X = 34.74$ mm and at $t = 32$ $\mu$ s.....	26
Figure 27. Profiles of maximum principal Cauchy stress in rods 7-NT and 7-T along $X = 34.74$ mm and at $t = 32$ $\mu$ s.....	26
Figure 28. Profiles of maximum Cauchy shear stress in rods 7-NT and 7-T along $X = 34.74$ mm and at $t = 32$ $\mu$ s.....	27
Figure A-1. An element of bent rod at time $t$ .....	31
Figure B-1. The quasi-static, plane-strain plate problem studied in section B.1: (a) the plate is cantilevered at one end and point loaded at the other, (b) free-body diagram, (c) bending moment diagram.....	36
Figure B-2. The mid-plane deflection field computed for rod 7-NT with LS-DYNA closely agrees with the analytical solution for a plate with 12-mm thickness.....	37
Figure B-3. The mid-plane deflection field computed for rod 7-T with LS-DYNA is bounded by the analytical solution for plates with 12-mm and 10.72-mm thickness and is closer to the latter.....	37
Figure B-4. The quasi-static plane strain problems studied in section B.2: rods 7-NT, 7-T, and 7-TE are each cantilevered at one end and point loaded at the other.....	38
Figure B-5. The profiles of rods 7-NT, 7-T, and 7-TE.....	39

---

## List of Tables

---

Table 1. Properties of WHA in its linearly elastic representation.....	9
Table 2. Peak values of $T_{xx}$ at $X = 34.74$ mm and $t = 32$ $\mu$ s.....	19
Table 3. Maximum values of $T_1$ at $X = 34.74$ mm and $t = 32$ $\mu$ s.....	27
Table B-1. Effective thicknesses of the three plates.....	39

INTENTIONALLY LEFT BLANK

---

## 1. Introduction

---

Kinetic energy penetrators are generally threaded in order to accommodate a sabot. We determined to explore the extent to which, and the mechanisms by which, such threading increases a rod's susceptibility to breakup under conditions of oblique impact.

Section 2 describes experiments in which small-scale rods composed of a 93.1% tungsten-4.7% nickel-2.2% cobalt (93.1W-4.7Ni-2.2Co) tungsten heavy alloy (WHA), with and without threads, were launched with a gas gun into 9.5-mm-thick rolled homogeneous armor (RHA) targets at 60 degrees' obliquity and a speed of 1300 m/s. Differences in breakup patterns of threaded and unthreaded rods were noted.

Section 3 describes finite element (FE) simulations of the elastic impact on a rigid surface at a speed of 10 m/s and 60 degrees' obliquity of a threaded and an unthreaded geometry used in the experiments. The goal was to investigate differences between the two rods in terms of patterns of elastic stress waves and of structural bending. These dynamic calculations were performed in plane strain with the LS-DYNA<sup>1</sup> code (Livermore Software Technology Corp., 2003) in explicit mode. In order to further explore differences in bending characteristics, we also performed static plane-strain analyses of each rod cantilevered at one end and point loaded at the other. These static calculations employed LS-DYNA in the implicit mode.

Our general finding is that the threads, by decreasing the effective thickness of the rod, lead to a greater degree of bending under oblique impact. Axial bending stresses therefore attain larger magnitudes in the threaded rod. The threads also lead to a locally more triaxial state of stress and thus to a greater departure from a state of pure bending. Furthermore, the maximum principal stress upon which a brittle tensile failure criterion can be based attains larger values in the threaded rod, particularly in the vicinity of the threads, than are attained anywhere in the unthreaded rod.

Our results are summarized and an assessment is provided in section 4.

---

## 2. Experimental Observations

---

WHA rods with the threaded geometries (see figures 1 and 2) were fired into 9.5-mm- (3/8-inch) thick RHA plates at 1300 m/s and 60 degrees' obliquity (figure 3). (*Obliquity* is defined as the angle between the projectile's trajectory and the normal to the target.) The length-to-diameter (*L/D*) ratio was 16.2 for rod 6A-T and 16.7 for rod 7-T. The rods used in the experiments were

---

<sup>1</sup>LS-DYNA, which is not an acronym, is a trademark of Livermore Software Technology Corp.

composed of a tungsten-nickel-cobalt alloy with the composition 93.1W-4.7Ni-2.2Co. All were machined from a single lot of stock material obtained from Aerojet Ordnance Tennessee, Inc.

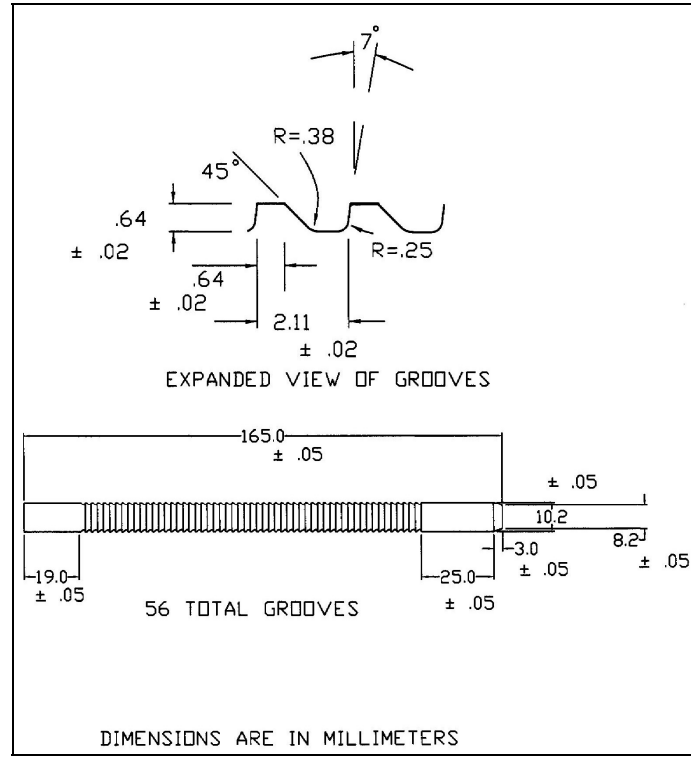


Figure 1. Geometry of rod 6A-T.

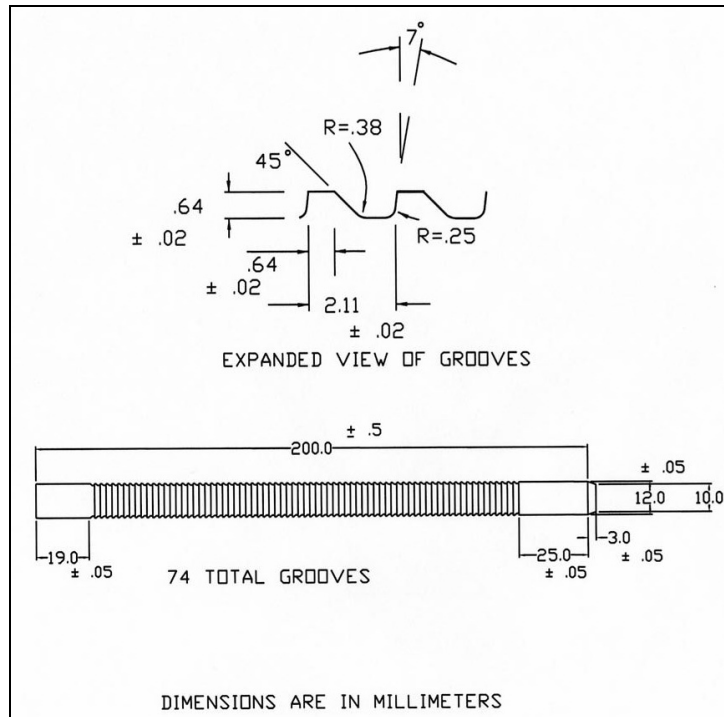


Figure 2. Geometry of rod 7-T.

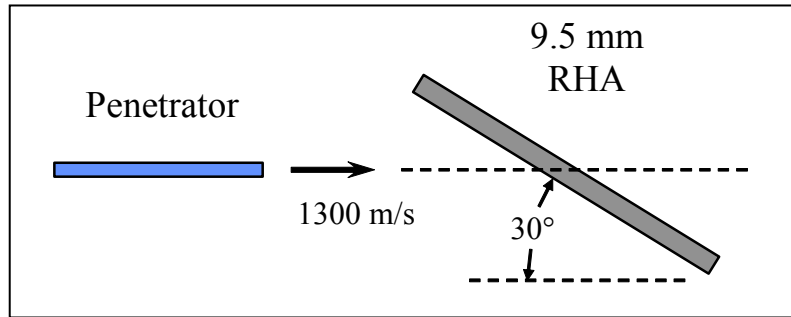


Figure 3. Sketch of the experiments; a tungsten rod strikes an RHA plate at 1300 m/s and 60 degrees' obliquity.

Five experiments were performed with the smaller rod, 6A-T. Figure 4 presents shadowgraphs at three post-perforation times from one of these experiments. The nose of the rod, extending from the front to a location between the third and fourth threads, has separated from the remainder as a single large fragment. A similar pattern was observed in the four other experiments with rod 6A-T.

Five ballistic experiments were also performed with the larger rod, 7-T. Figure 5 presents shadowgraphs at three post-perforation times from one of these experiments. The pattern is quite similar to that noted in figure 4, namely, the nose of the rod has separated as a single large fragment, this time at a location between the seventh and eighth threads. Three of the four other experiments involving rod 7-T also displayed the pattern in figure 5 of separation of the nose region as a single large fragment. Shadowgraphs from the remaining experiment with 7-T are shown in figure 6. Here, fragmentation is seen to have occurred at several locations. We speculate that some pre-impact yaw may have been present in the experiment of figure 6.

The post-perforation shadowgraphs in figure 7 show rod 7-NT, identical in geometry to 7-T but without threads, in four different experiments. These small-scale prototype rods were launched without a sabot by means of a pusher plate, which made testing of the 7-NT possible. Results with 7-NT displayed greater experiment-to-experiment variability than did results with the two threaded geometries. Two of four experiments (figures 7a and 7b) displayed the pattern familiar from experiments with the threaded rods, namely, separation of a single fragment from the nose region. In one of the four experiments (figure 7c), the rod fragmented into two pieces near its center. In the remaining experiment with 7-NT (figure 7d), the rod remained intact. On the basis of this fourth experiment, we draw the conclusion that the presence of threading increases the susceptibility of tungsten rods to fracture under conditions of oblique impact.

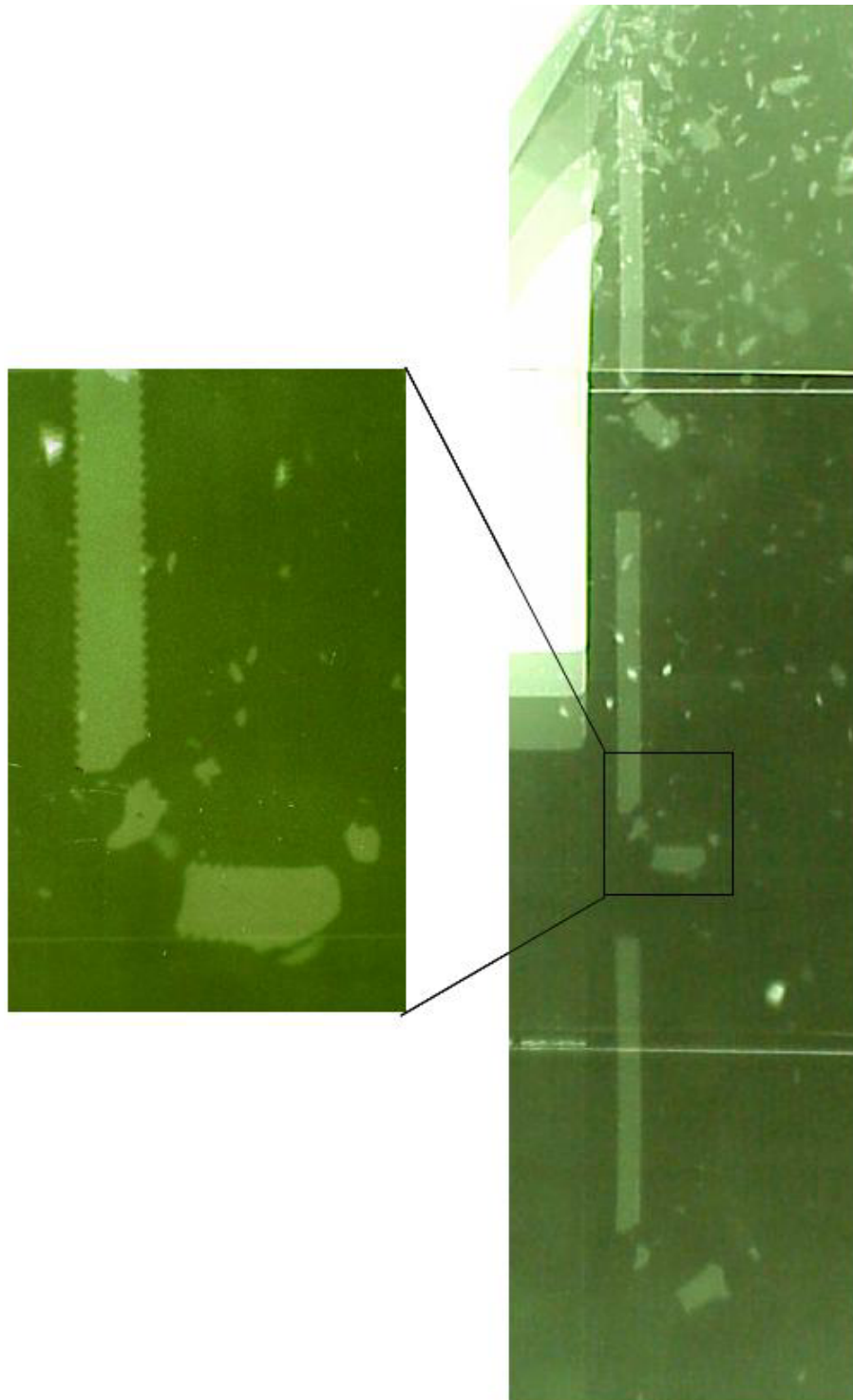


Figure 4. Shadowgraphs of rod 6A-T at three times following perforation of an RHA plate; this pattern of separation of a single large nose fragment occurred in all five experiments with 6A-T.

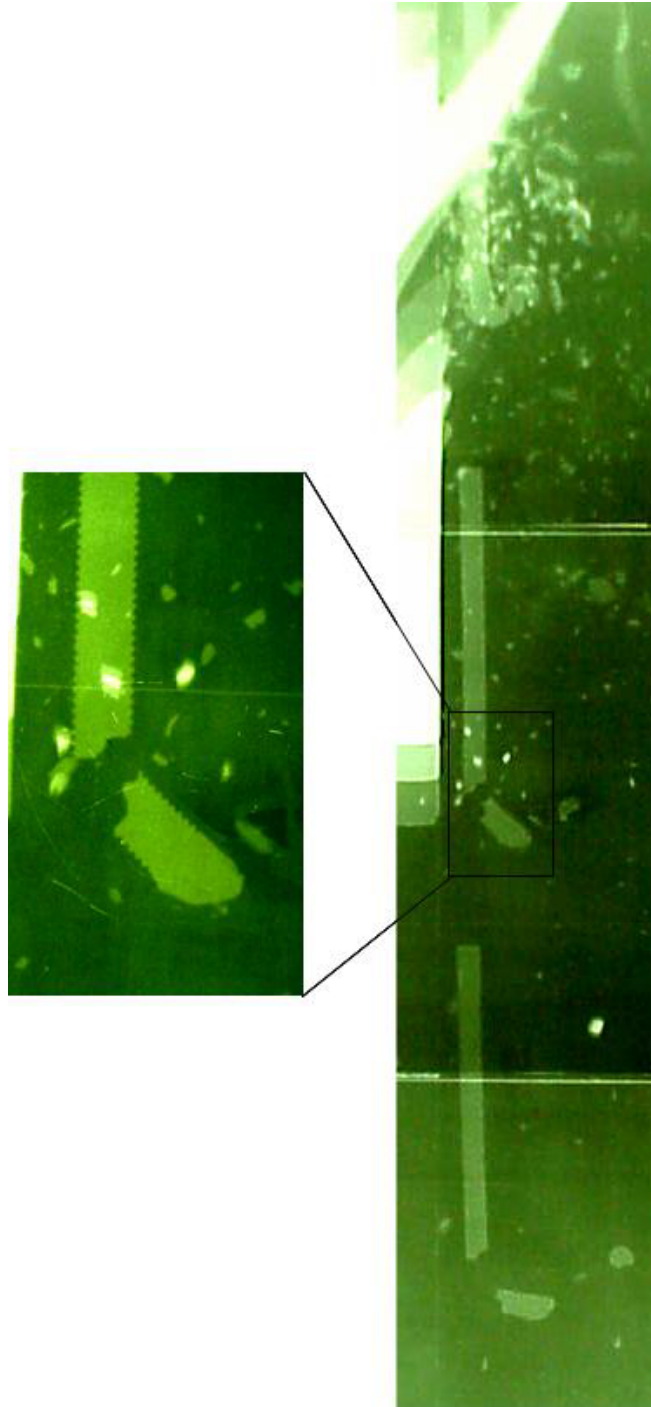


Figure 5. Shadowgraphs of rod 7-T at three times following perforation of an RHA plate; this pattern of separation of a single nose fragment was repeated in four of five experiments with 7-T.

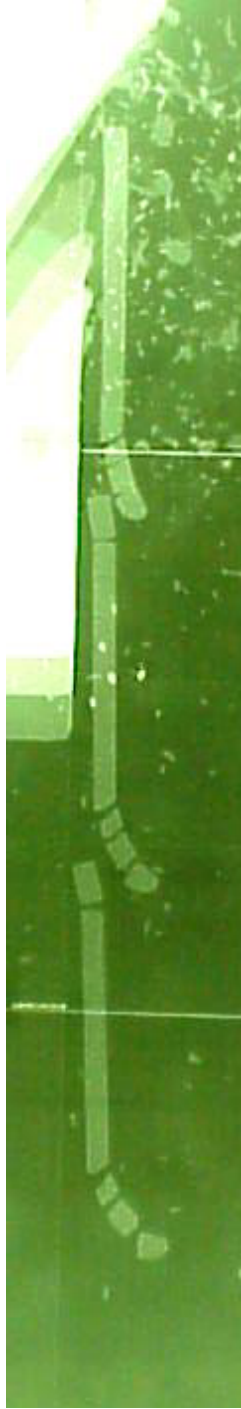


Figure 6. Shadowgraphs of rod 7-T at three times following perforation of an RHA plate from the single experiment in which 7-T fragmented at multiple locations.

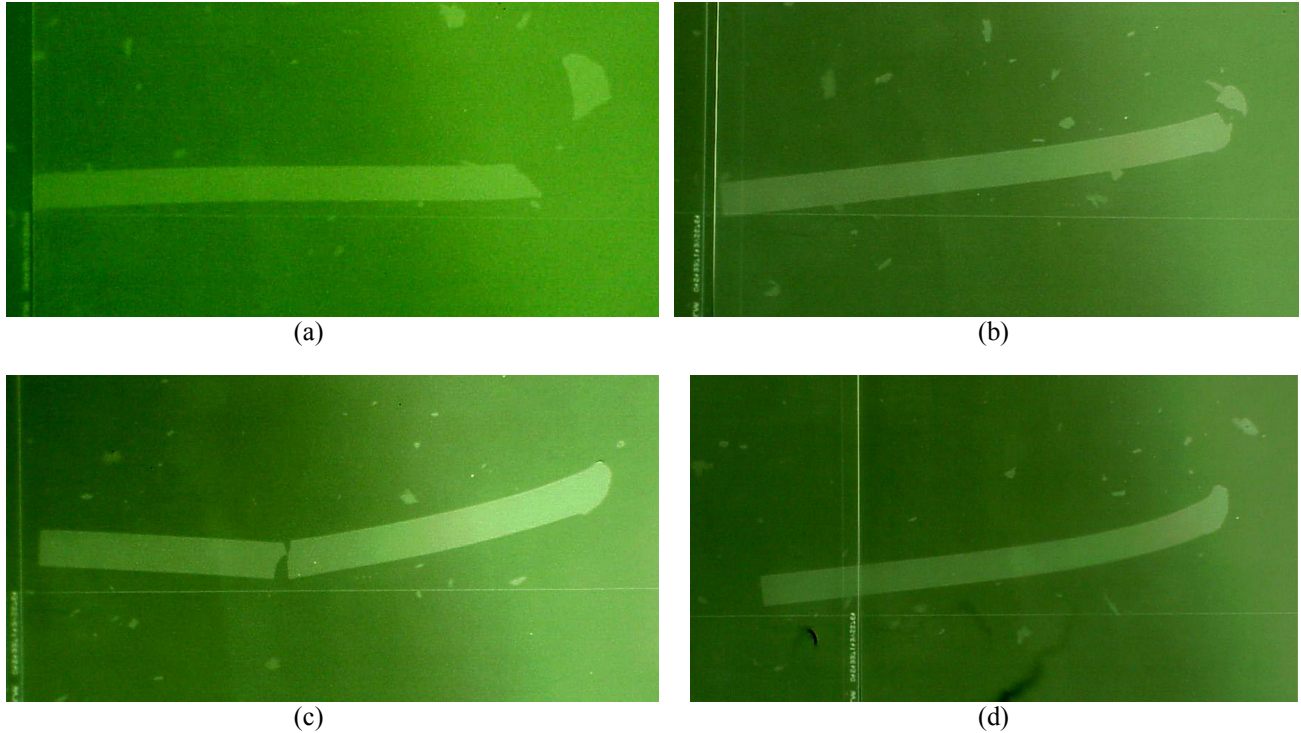


Figure 7. A post-perforation shadowgraph of rod 7-NT from each of four experiments; the results show greater experiment-to-experiment variability than with 6A-T and 7-T, and in one experiment, the rod remained intact.

---

### 3. Plane-Strain Modeling of Oblique Impact

---

#### 3.1 Problem Definition

The goal of our finite element modeling was to explore sources of the increased fracture susceptibility associated with threading. We decided to pursue an elastic plane-strain analysis of rod 7 in figure 2, both threaded (7-T) and unthreaded (7-NT). The possibility for inherently three-dimensional (3-D) and/or inelastic sources for increased fracture susceptibility can be explored in more costly, future analyses outside the scope of this report. In the present report, we are pursuing the hypothesis that increased *bending* in the threaded rod, compared to the unthreaded rod, accounts, at least in part, for its increased tendency to fragment under oblique impact. This phenomenon can be isolated and studied in its simplest form in this two-dimensional (2-D) elastic model.

Figure 8 shows the problem that we analyzed. This problem is simpler yet relevant to that of figure 3 which we studied experimentally. The RHA target has been replaced by a rigid surface, still inclined at 30 degrees to the rod's initial trajectory. A state of plane strain is assumed for both the rod and plate. The rod's impact speed has been reduced to 10 m/s in order to keep the results linear and elastic.

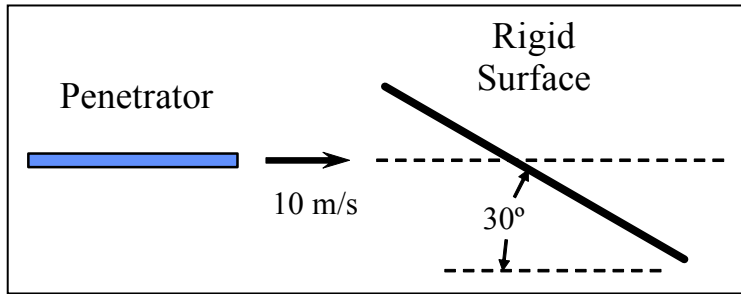


Figure 8. Sketch of the plane-strain problems studied in section 3: a tungsten rod strikes a rigid target at 10 m/s and 60 degrees' obliquity.

Figure 9 shows the front portion of rod 7-T and indicates the material and spatial reference frames and Cartesian coordinate systems employed in our analyses. Our material coordinates,  $(X, Y, Z)$ , specify a material point's location at time  $t = 0$ . The origin,  $X = Y = 0$ , coincides with the central point on the front edge of the rod. Coordinate  $X$  measures distance along the rod, and  $Y$  measures distance above and below the mid-plane of the rod. At  $t = 0$ , the  $x, y$ , and  $z$  axes of our fixed spatial coordinate system coincide with the  $X, Y$ , and  $Z$  axes, respectively. Motion and deformation are assumed to be confined to the  $x$ - $y$  plane.

The LS-DYNA finite element code was applied in its explicit mode to all calculations in section 3. The rigid surface inclined at 30 degrees to the  $x$ -axis was specified with the use of the feature `*RIGIDWALL_GEOMETRIC_FLAT`.

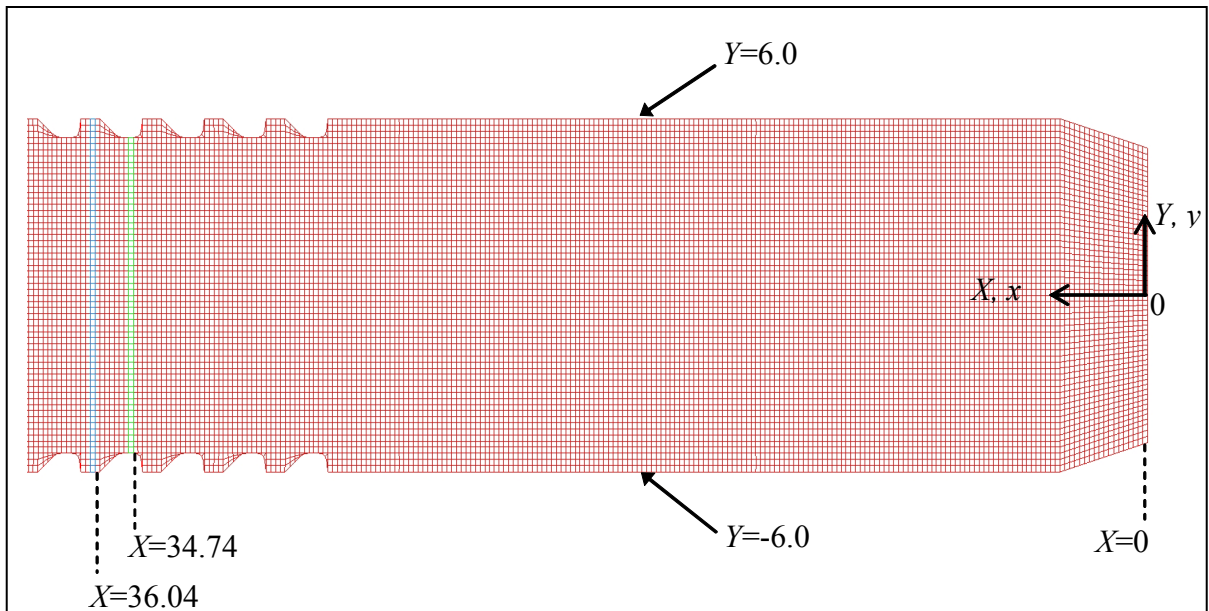


Figure 9. The front portion of rod 7-T, with material and spatial coordinate systems indicated (dimensions are in millimeters).

### 3.2 Meshes

We used AutoCAD LT<sup>2</sup> (Autodesk<sup>2</sup> Corporation, 2005) to create geometry files in “dxf” format for rods 7-NT and 7-T. In the latter case, the 2-D cross-sectional geometry shown in figure 2, including the thread details, was accurately represented.

These “dxf” files were then imported into HyperMesh<sup>3</sup> (Altair<sup>3</sup> Engineering, Inc., 2005) to create the meshes shown in figures 10 and 11 for rods 7-T and 7-NT, respectively. Our restriction to 2-D plane strain allowed for the small element size of about 0.2 mm to be used throughout the mesh. The mesh for 7-T contained 71,038 nodes and 69,898 elements. Almost all these elements were four-node quadrilaterals. A small number of three-node triangles was employed in the vicinity of each thread. The mesh for 7-NT consisted of 72,689 nodes and 71,398 elements; here, all the elements were four-node quadrilaterals. The meshes were exported from HyperMesh in LS-DYNA format.

In LS-DYNA, \*SECTION\_SHELL with ELFORM=13 was used to specify plane strain. Reduced integration (one Gaussian quadrature point per element) was employed.

### 3.3 WHA Properties

The rods used in the experiments were composed of a tungsten-nickel-cobalt alloy with the composition 93.1W-4.7Ni-2.2Co. The properties assigned in the finite element analyses are listed in table 1. The value for density  $\rho$  was reported in Johnson (1993) for a tungsten-nickel-Fe alloy with composition 90W-7Ni-3Fe. In our low-velocity impact calculations, the WHA was assumed to behave as a homogeneous, isotropic, linearly elastic continuum. The values used for its elastic Young’s modulus  $E$  and Poisson’s ratio  $\nu$  are also listed in table 1. In LS-DYNA, Material \*MAT\_ORTHOTROPIC\_ELASTIC was applied to the WHA in the degenerate isotropic case.

Table 1. Properties of WHA in its linearly elastic representation.

$\rho$ (kg/m <sup>3</sup> )	$E$ (GPa)	$\nu$
16980	327.4	0.3193

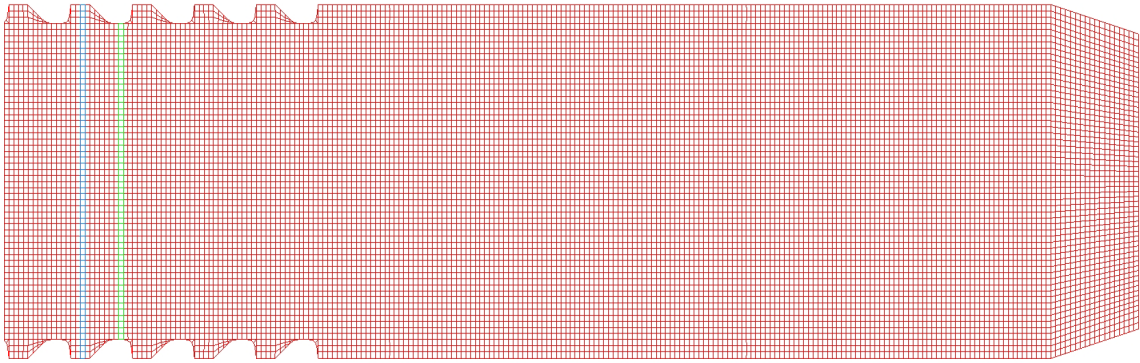
---

<sup>2</sup>AutoCAD LT and Autodesk are registered trademarks of Autodesk Corporation.

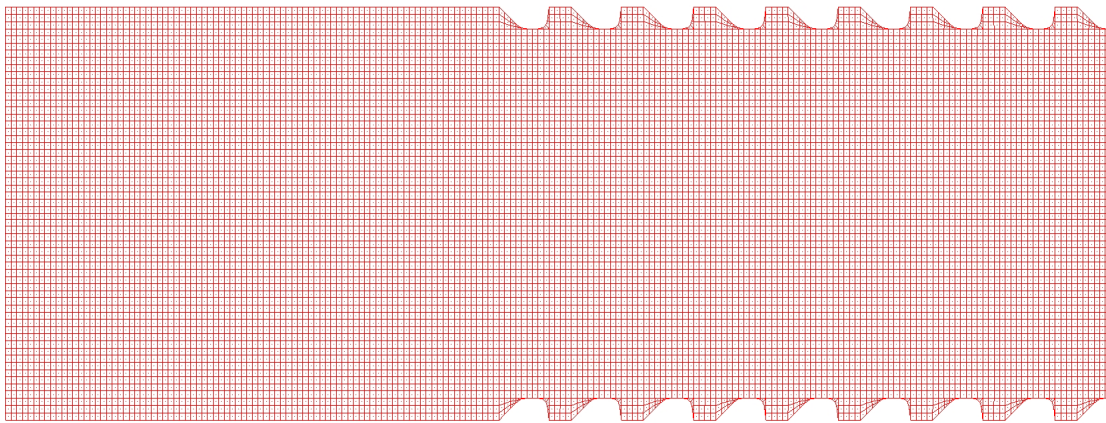
<sup>3</sup>HyperMesh and Altair are registered trademarks of Altair Engineering, Inc.



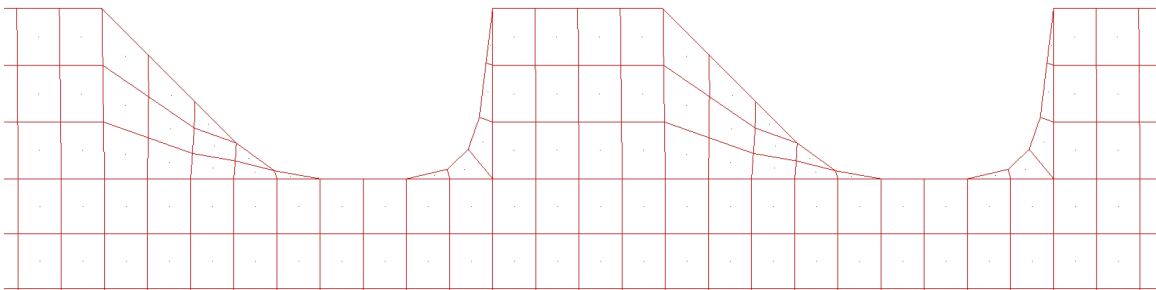
(a)



(b)



(c)



(d)

Figure 10. FE mesh for rod 7-T, (a) overview, (b) front, (c) back, (d) thread.

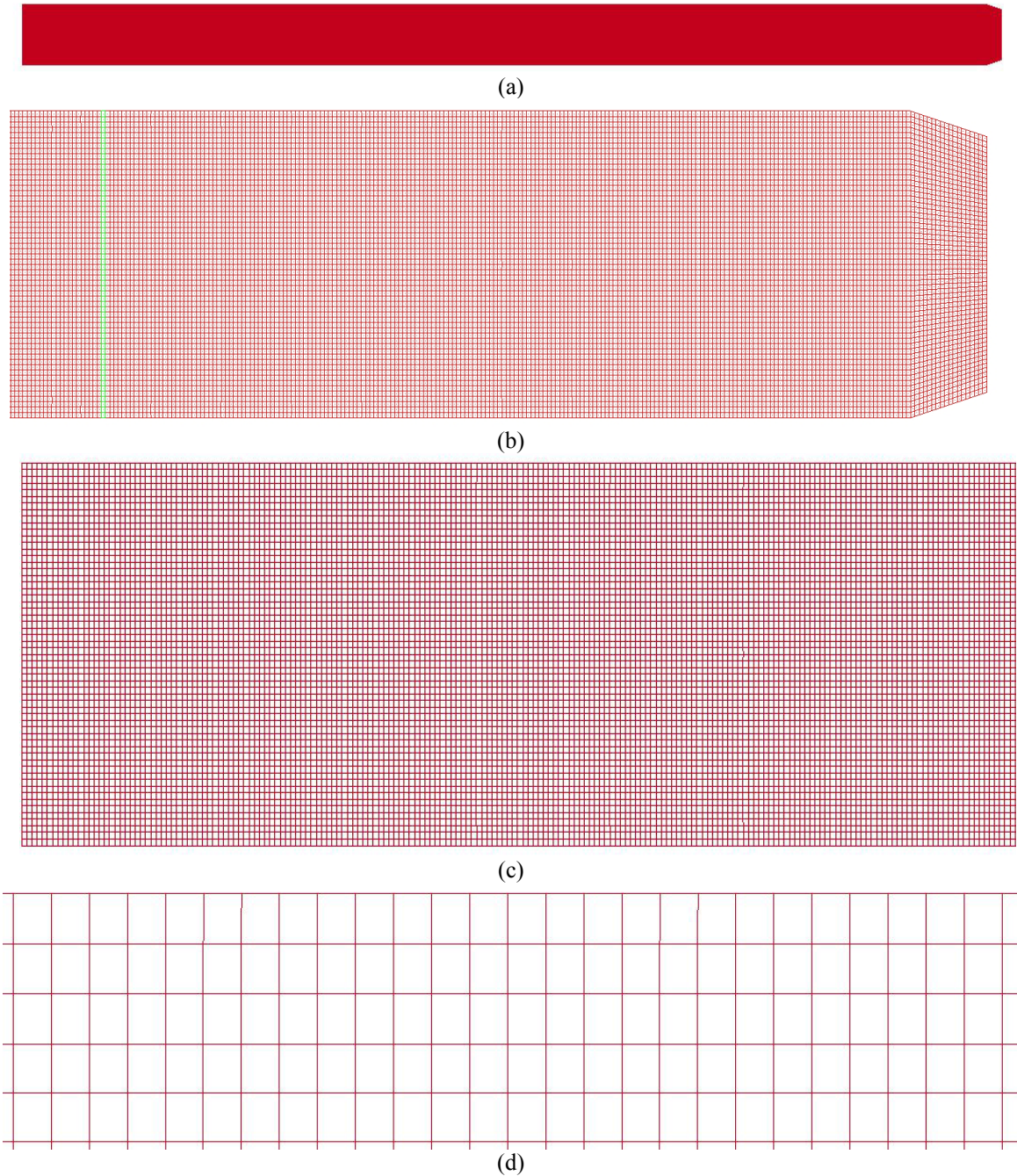


Figure 11. FE mesh for rod 7-NT, (a) overview, (b) front, (c) back, (d) “top”.

### 3.4 Results and Discussion

#### 3.4.1 Contour Plots of $T_{xx}$ Throughout Rods 7-NT and 7-T

Figures 12 and 13 show contours of the Cauchy stress component  $T_{xx}$  at 5- $\mu$ s intervals throughout the entire rod 7-NT. Figures 14 and 15 do the same for rod 7-T. Time is measured from the instant of initial impact on the rigid surface.  $T_{xx}$  is resolved in terms of the fixed  $x$ -axis direction,

but since little rigid-body rotation occurs during the 100  $\mu\text{s}$  covered in these figures,  $T_{xx}$  can be closely identified with the rod's axial stress. "Red" indicates axial tension and "blue" indicates axial compression. Note that the scale is very sensitive, with a full range of  $\pm 10$  MPa.

Figures 12 and 14 show an initial "blue" axial compression wave that traverses the 200-mm length of the rod in about 43  $\mu\text{s}$ . This traversal time corresponds very closely to speed  $\sqrt{E/(1-\nu^2)\rho}$  or 4634 m/s with properties in table 1. This wave speed is derived with the assumption, in addition to plane strain, that  $T_{yy}$  and  $T_{xy}$  are approximately zero throughout the rod. The motivation for this assumption is that  $T_{yy}$  and  $T_{xy}$  are zero on the bounding free surfaces at the maximum and minimum  $Y$  values and the rod is thin (see Kolsky, 1963, pp. 79-83).

In the wake of the axial compression wave, figures 12 and 14 show a slower traveling region of alternating tension and compression on either side of the rod's mid-surface. This is a characteristic bending pattern, in which the rod is axially extended on one side of its neutral surface and axially compressed on the other. The slower wave is therefore a flexural wave. In appendix A, we derive a condition on the flexural wavelength in order for the flexural wave to move more slowly than the axial compression wave. At later times, in figures 13 and 15, the entire rod is in a standing-wave pattern of flexure.

### 3.4.2 History Plots of $T_{xx}$ in Rods 7-NT and 7-T at $X = 34.74$ mm

Figure 16 presents a family of plots of  $T_{xx}$  at  $X = 34.74$  mm as functions of time for rod 7-NT. Figure 17 presents the same for rod 7-T. The strip of elements with centroid location  $X = 34.74$  mm is shown in "green" in figures 9, 10b, and 11b. In rod 7-T, this strip intersects the two free surfaces at the approximate center of the trough between threads 3 and 4. Each plot in the family corresponds to a particular value of  $Y$ . The FE solution has been sampled at a  $Y$ -interval of every three elements, or about 0.6 mm. In each figure, the curves at  $Y = \pm 0.31$  mm pertain to elements closest to the rod's mid-surface. In figure 16,  $Y = \pm 5.89$  mm pertains to elements having one edge on rod 7-NT's free surface at  $Y = \pm 6.00$  mm. In figure 17,  $Y = \pm 5.26$  mm pertains to elements having one edge on rod 7-T's free surface at  $Y = \pm 5.36$  mm.

In both figures, every plot attains a local and perhaps a global extremum at about 32  $\mu\text{s}$  after initial impact. These early-time extrema are of particular interest because our results for impact on a rigid surface (figure 8) are of greatest relevance to the RHA perforation problem of figure 3 at early times. The remaining analysis therefore focuses on this particular time.

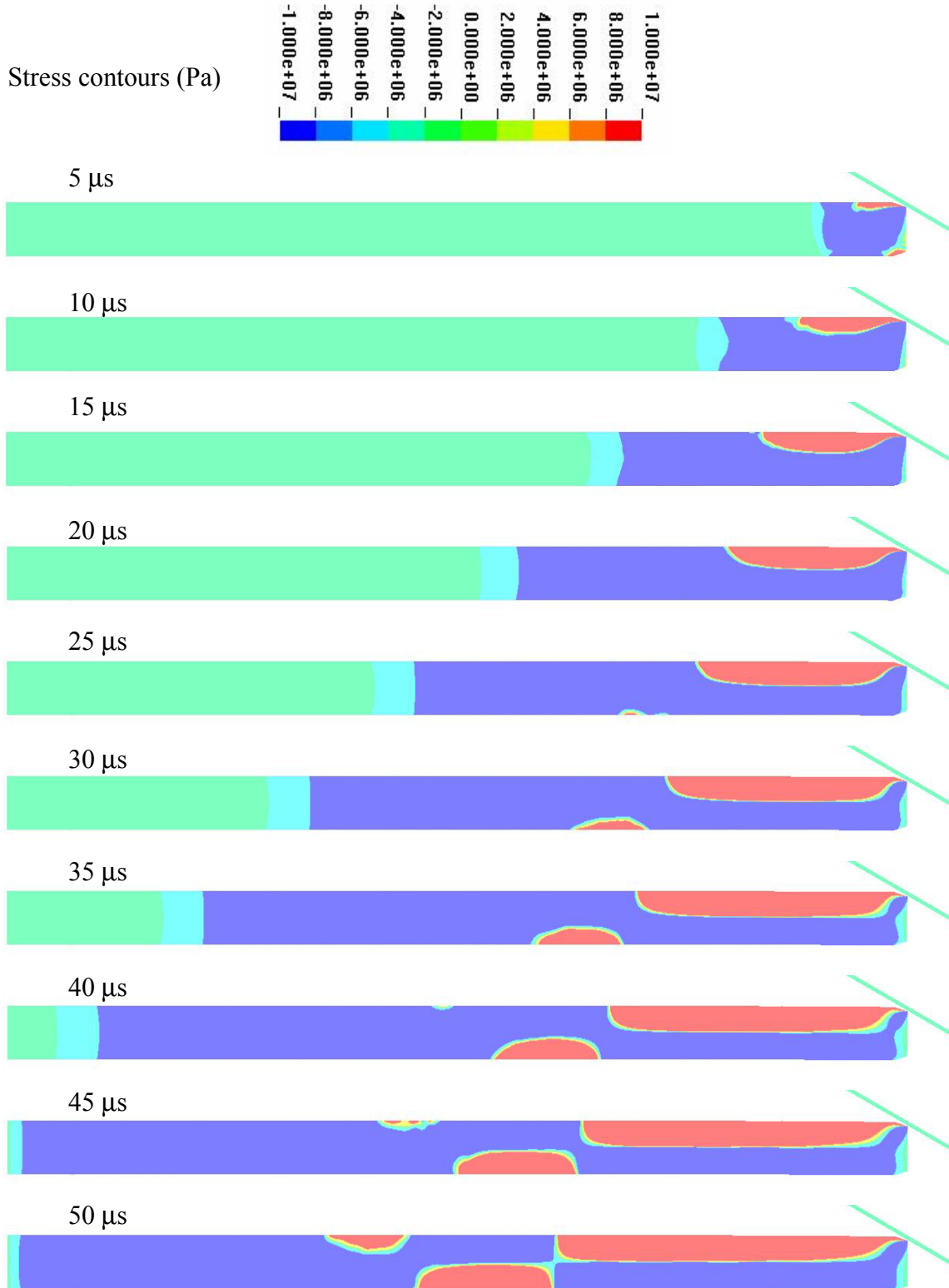


Figure 12.  $T_{xx}$  in rod 7-NT at specific times in the range of 5 to 50  $\mu$ s after impact.



Figure 13.  $T_{xx}$  in rod 7-NT at specific times in the range of 55 to 100  $\mu$ s after impact.

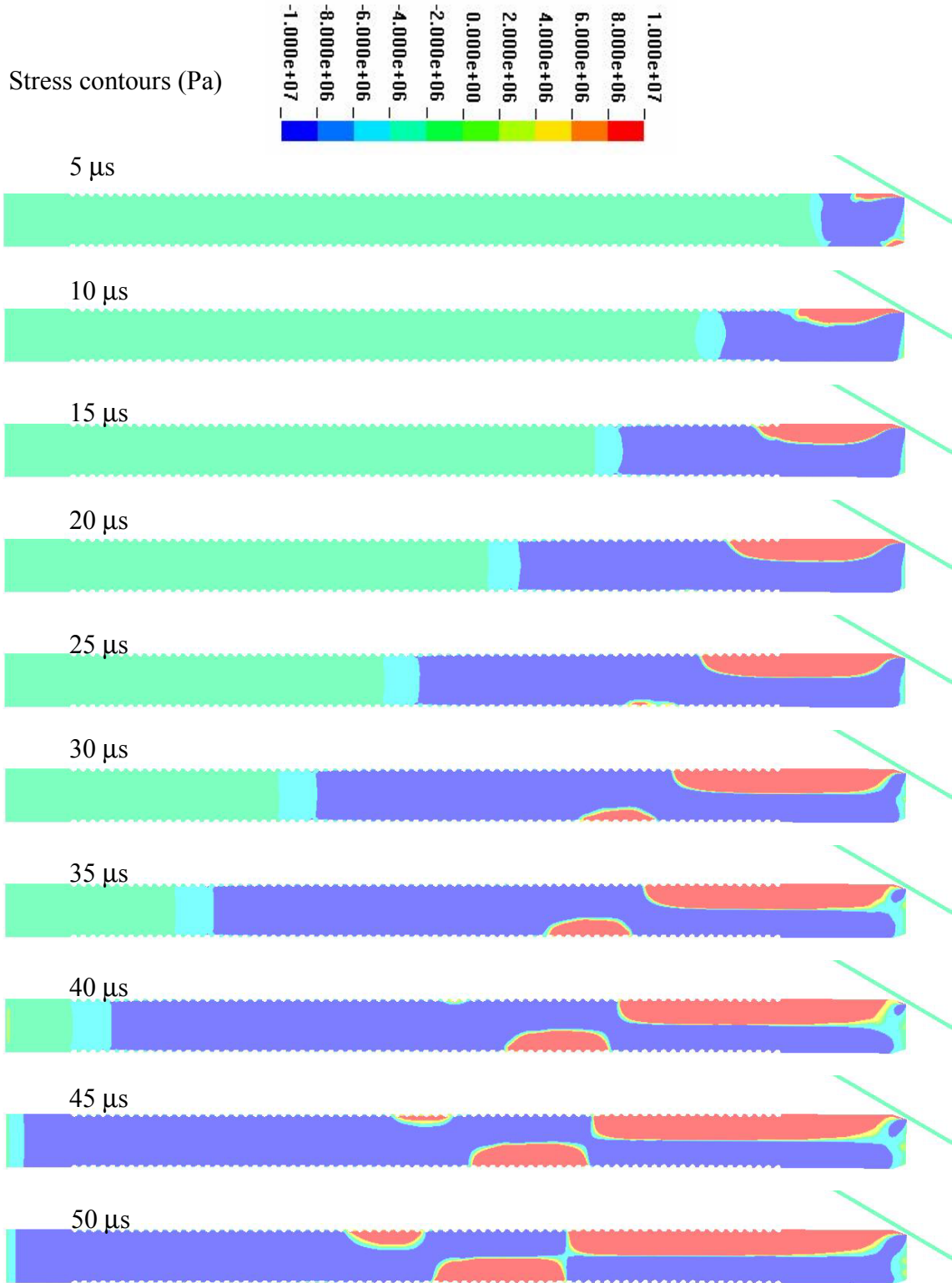


Figure 14.  $T_{xx}$  in rod 7-T at specific times in the range of 5 to 50  $\mu$ s after impact.



Figure 15.  $T_{xx}$  in rod 7-T at specific times in the range of 55 to 100  $\mu$ s after impact.

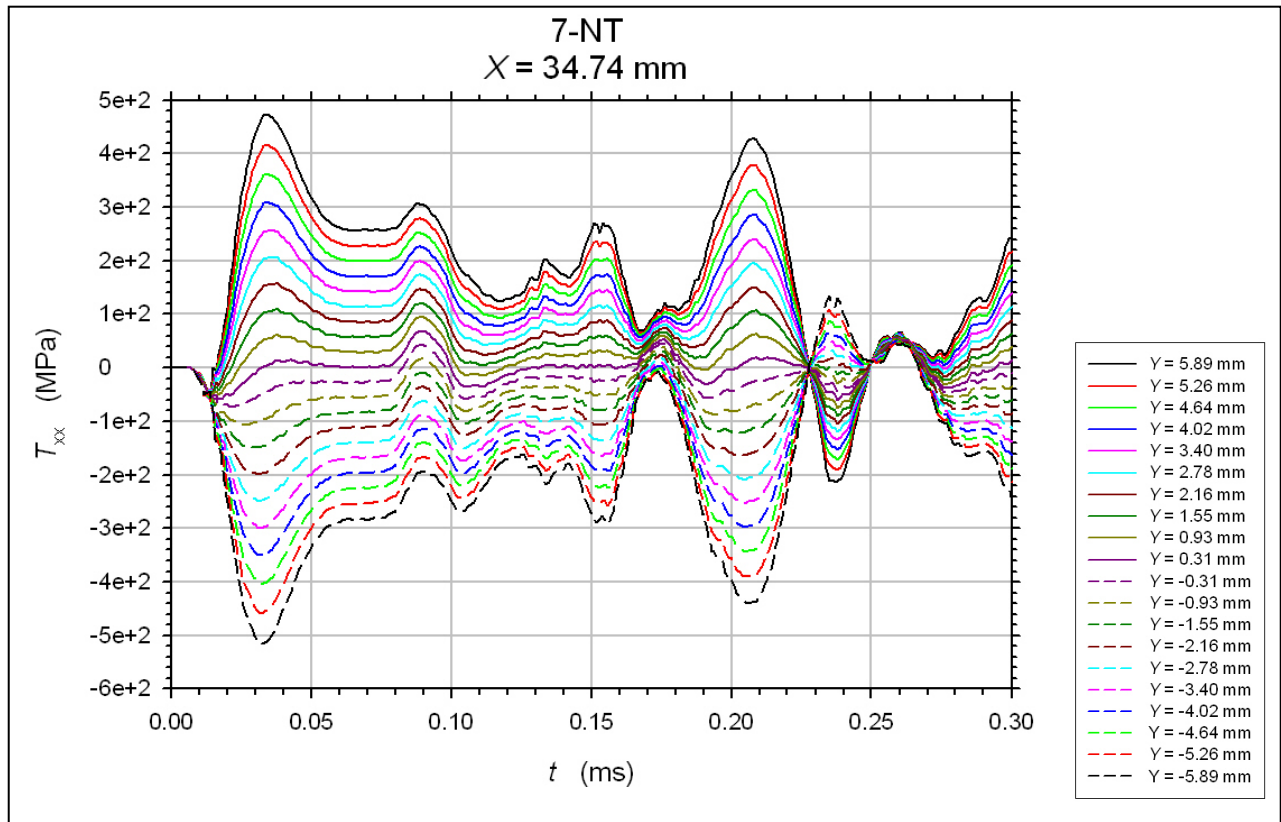


Figure 16.  $T_{xx}$  in rod 7-NT along  $X = 34.74$  mm as a function of time after impact. (Note the peaks at  $t \cong 32 \mu\text{s}$ .)

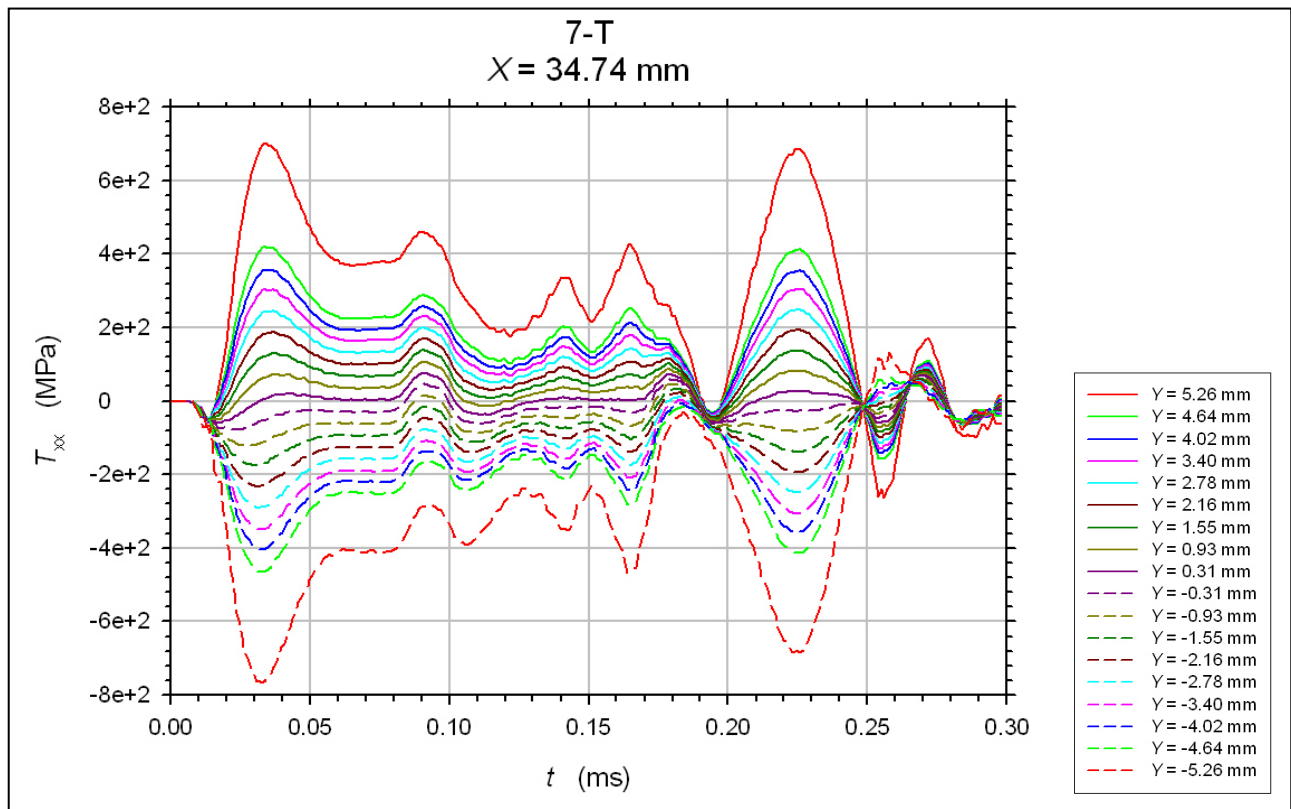


Figure 17.  $T_{xx}$  in rod 7-T along  $X = 34.74$  mm as a function of time after impact. (Note the peaks at  $t \cong 32 \mu\text{s}$ .)

### 3.4.3 Profiles of $T_{xx}$ , $T_{yy}$ , $T_{zz}$ , and $T_{xy}$ in Rods 7-NT and 7-T at $X = 34.74$ mm and $t = 32$ $\mu$ s

Plots of  $T_{xx}$ ,  $T_{yy}$ ,  $T_{zz}$ , and  $T_{xy}$  as functions of  $Y$  (“ $Y$ -profiles”) for  $X = 34.74$  mm and  $t = 32$   $\mu$ s are given in figure 18 for rod 7-NT. In appendix A, we describe a state of *pure bending*, in which the plate is bent into locally circular arcs and  $T_{xx}$  increases linearly with distance  $Y$  from the neutral surface (see equation A-2). The neutral surface can be identified with the mid-plane in the case of our symmetric geometries. Figure 18 shows that a state of pure bending closely approximates our solution for rod 7-NT. Note the small negative offset from zero in  $T_{xx}$  at  $Y = 0$ , which is indicative of a small superimposed axial compression.

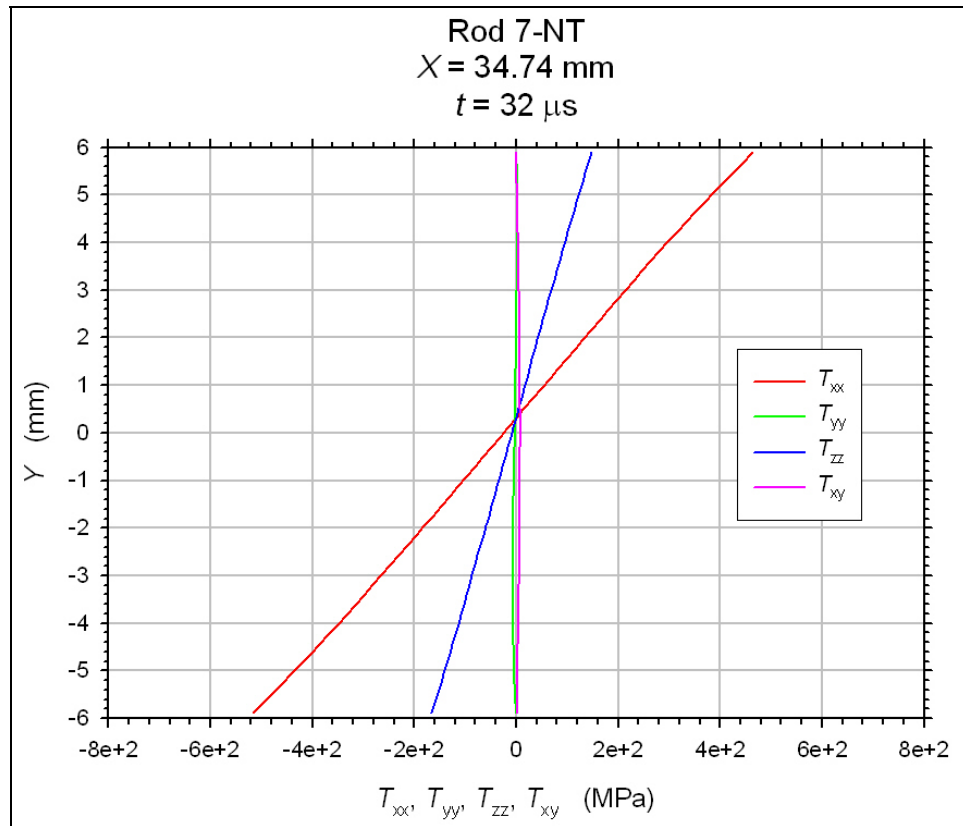


Figure 18. Profiles of  $T_{xx}$ ,  $T_{yy}$ ,  $T_{zz}$ , and  $T_{xy}$  in rod 7-NT along  $X = 34.74$  mm and at  $t = 32$   $\mu$ s.

$Y$ -profiles of  $T_{xx}$ ,  $T_{yy}$ ,  $T_{zz}$ , and  $T_{xy}$  for  $X = 34.74$  mm and  $t = 32$   $\mu$ s are shown in figure 19 for rod 7-T. Figure 19 shows that rod 7-T was also approximately in a state of pure bending within its central core region bounded by  $Y \cong \pm 4.5$  mm. Outside this core region, in the vicinity of the threads, two observations can be made for rod 7-T, based on figure 19. First,  $T_{xx}$  increases steeply with further increases in  $Y$ , and second, a more triaxial state of stress develops as  $T_{yy}$ ,  $T_{zz}$ , and  $T_{xy}$  all increase substantially in absolute value (but remain smaller in absolute value than  $T_{xx}$ ).

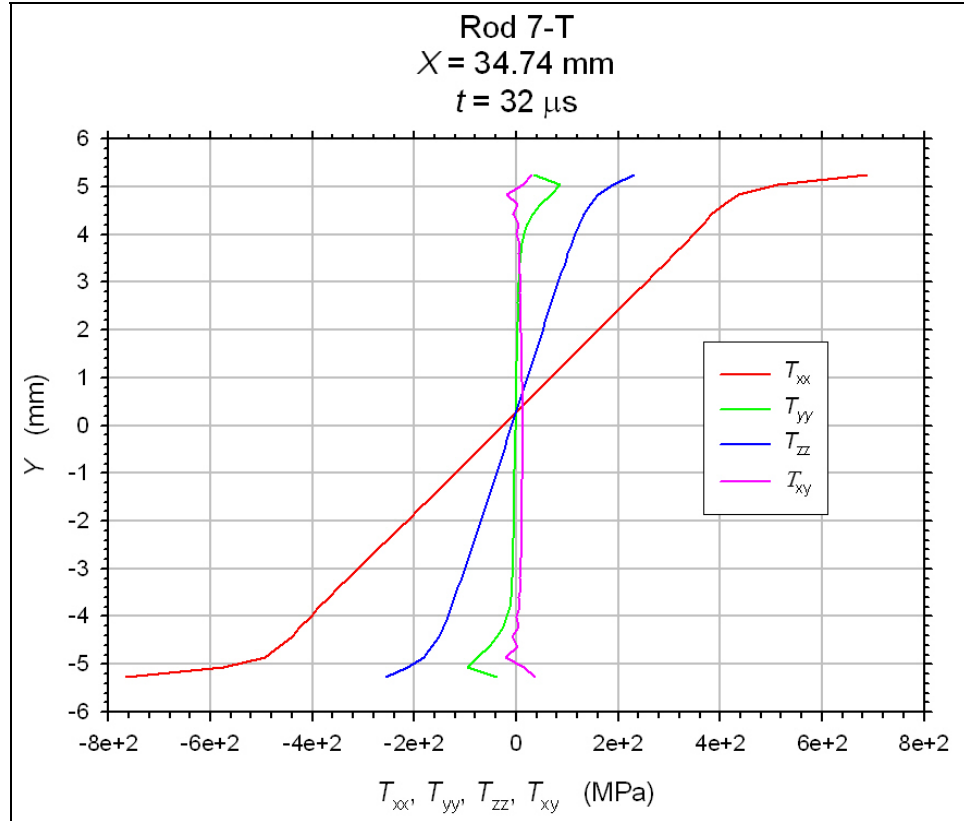


Figure 19. Profiles of  $T_{xx}$ ,  $T_{yy}$ ,  $T_{zz}$ , and  $T_{xy}$  in rod 7-T along  $X = 34.74$  mm and at  $t = 32$  μs.

$Y$ -profiles of  $T_{xx}$  at  $X = 34.74$  mm and  $t = 32$  ms for rods 7-NT and 7-T are compared in figure 20. The 7-NT and 7-T results intersect at  $T_{xx} = -16$  MPa, offset from zero because of the superimposed axial compression. Note that with the exception of the immediate vicinity of this single intersection point,  $|T_{xx}|$  is greater in rod 7-T than in 7-NT. In rod 7-T,  $T_{xx}$  attains its maximum of 688 MPa at  $Y = 5.26$  mm and its minimum of  $-766$  MPa at  $Y = -5.26$  mm. In rod 7-NT,  $T_{xx}$  attains its maximum of 463 MPa at  $Y = 5.89$  mm and its minimum of  $-517$  MPa at  $Y = -5.89$  mm. These observations are collected in table 2.

Table 2. Peak values of  $T_{xx}$  at  $X = 34.74$  mm and  $t = 32$  μs.

rod 7-NT				rod 7-T			
max (MPa)	at $Y$ (mm)	min (MPa)	at $Y$ (mm)	max (MPa)	at $Y$ (mm)	min (MPa)	at $Y$ (mm)
463	5.89	-517	-5.89	688	5.26	-766	-5.26

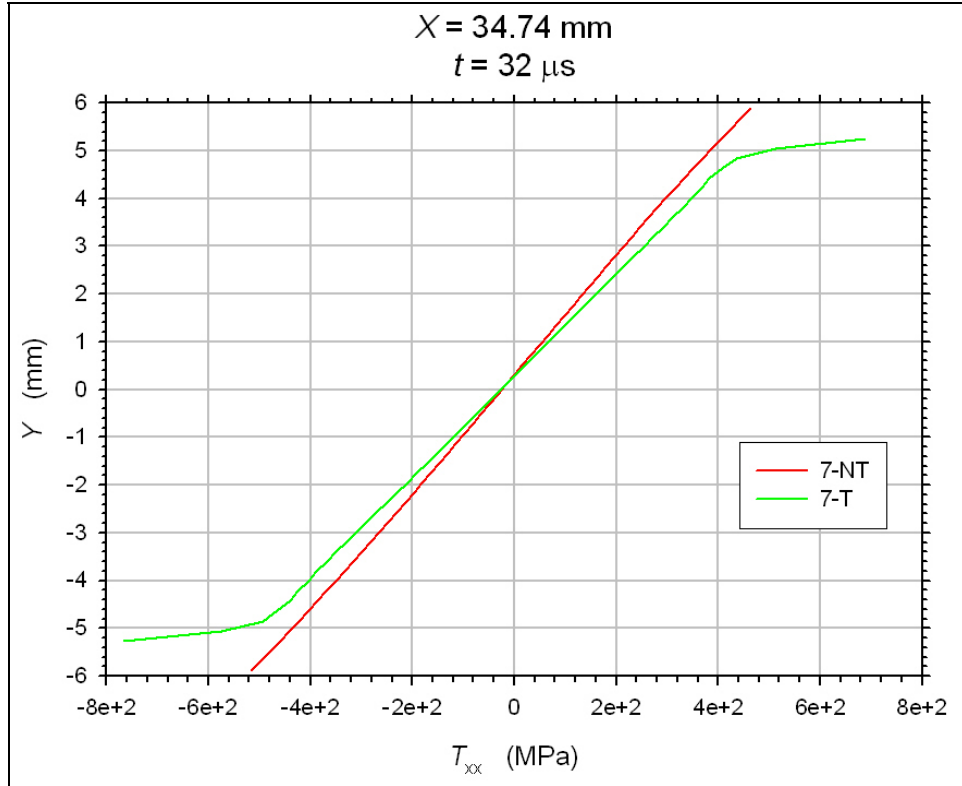


Figure 20. Profiles of  $T_{xx}$  in rods 7-NT and 7-T along  $X = 34.74 \text{ mm}$  and at  $t = 32 \mu\text{s}$ .

### 3.4.4 Contour Plots of $T_{xx}$ in Rod 7-T in the Vicinity of Threads 1 Through 8

Figures 21 and 22 show  $T_{xx}$  contours in rod 7-T in the vicinity of the first eight threads. Note the reduced contour sensitivity; in figures 21 and 22, the full range is  $\pm 200 \text{ MPa}$ , whereas in figures 12 through 14, it was  $\pm 10 \text{ MPa}$ .

The contours in figures 21 and 22 clearly show the threads' interiors to be at a lower level of axial stress than in the central core of the rod. This is not surprising since the stress-free boundary conditions require  $T_{xx}$  to be zero on all three faces of each thread.

### 3.4.5 History Plots of $T_{xx}$ in Rod 7-T at $X = 36.04 \text{ mm}$

In rod 7-T, the location  $X = 36.04 \text{ mm}$  corresponds to the approximate center of the fourth thread (figure 9). Figure 23 contains a family of plots of  $T_{xx}$  at this  $X$  location in rod 7-T as functions of time. The FE solution has again been sampled at a  $Y$ -interval of every three elements, or about  $0.6 \text{ mm}$ .

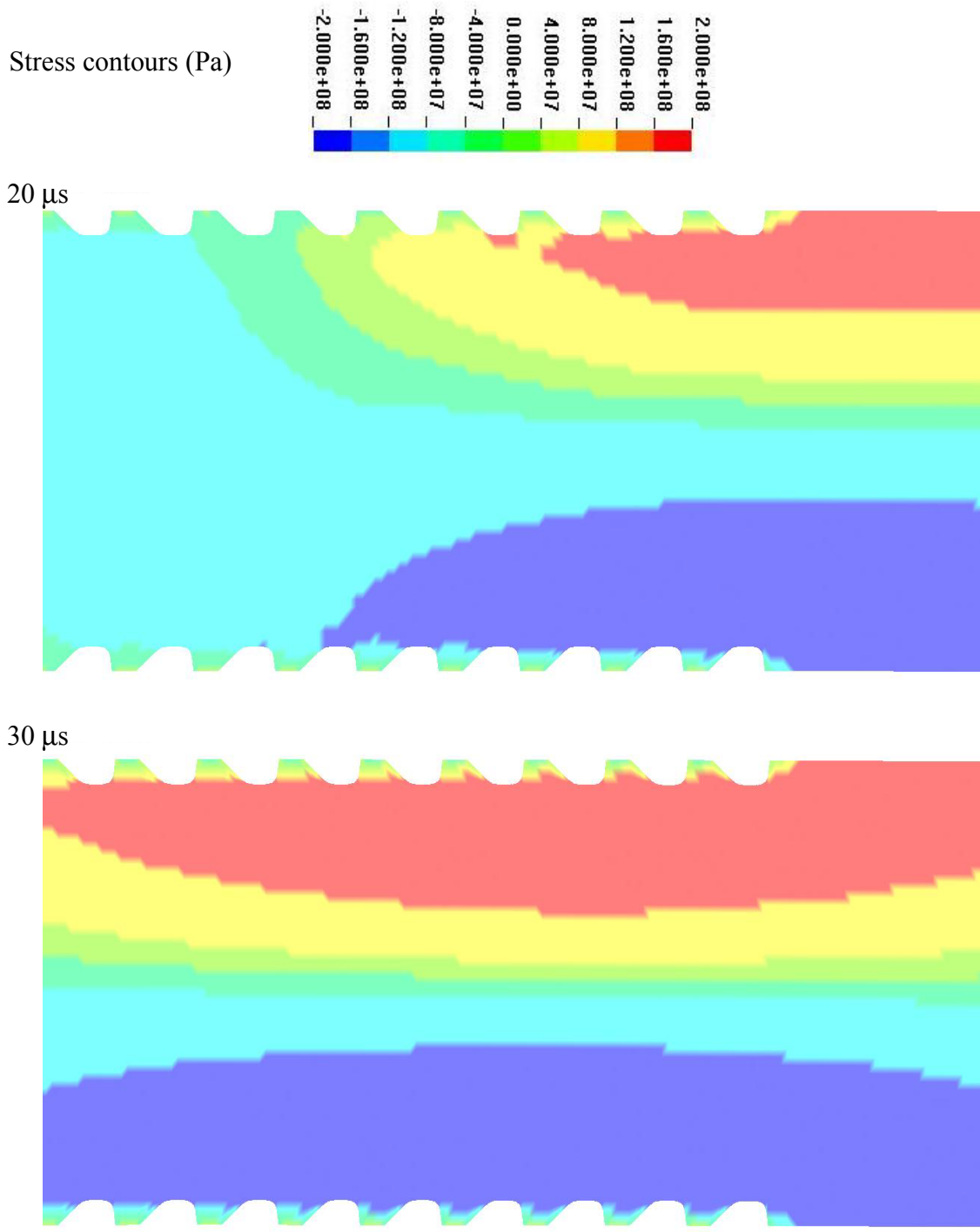


Figure 21.  $T_{xx}$  in rod 7-T at 20 and 30  $\mu$ s after impact.

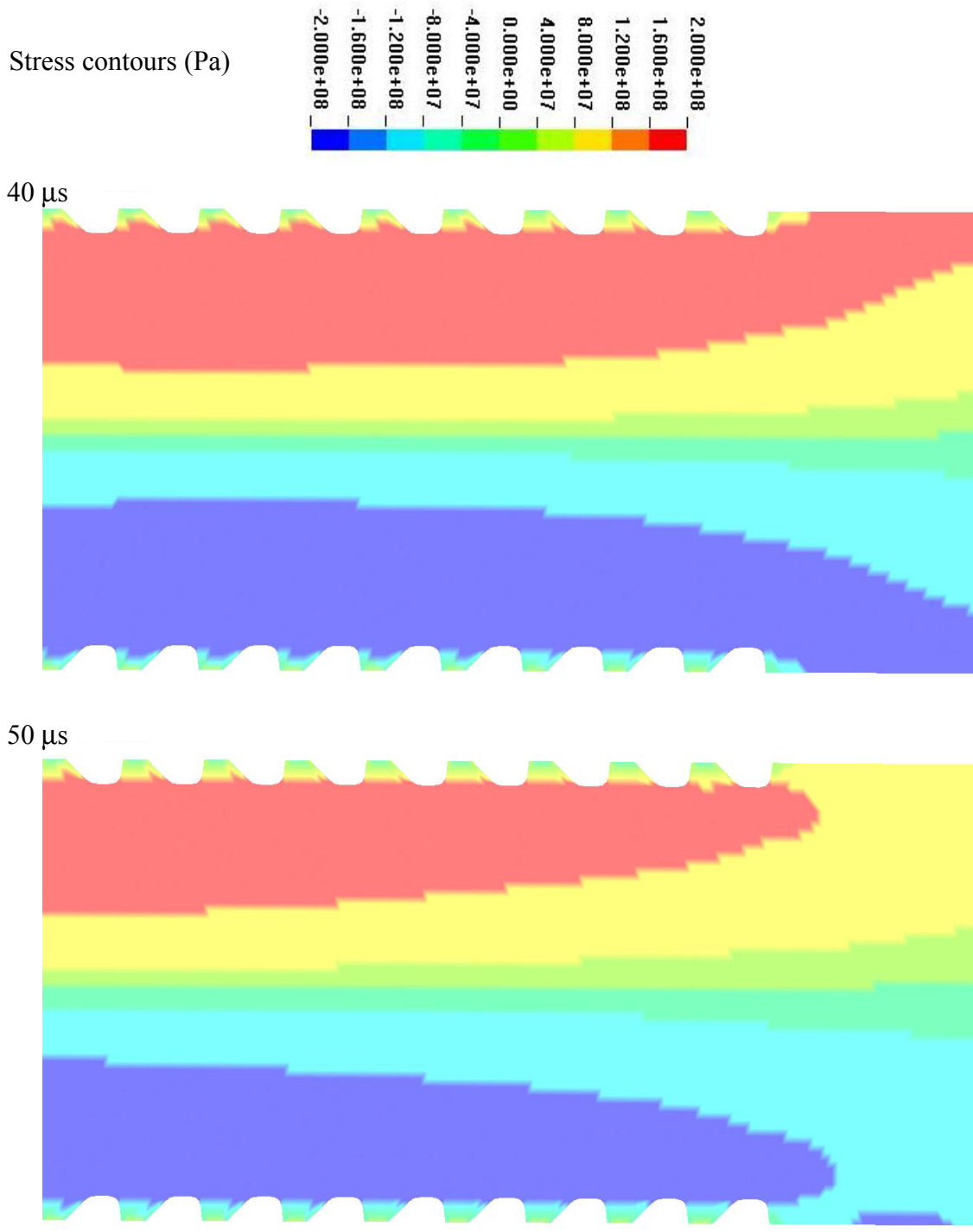


Figure 22.  $T_{xx}$  in rod 7-T at 40 and 50  $\mu$ s after impact.

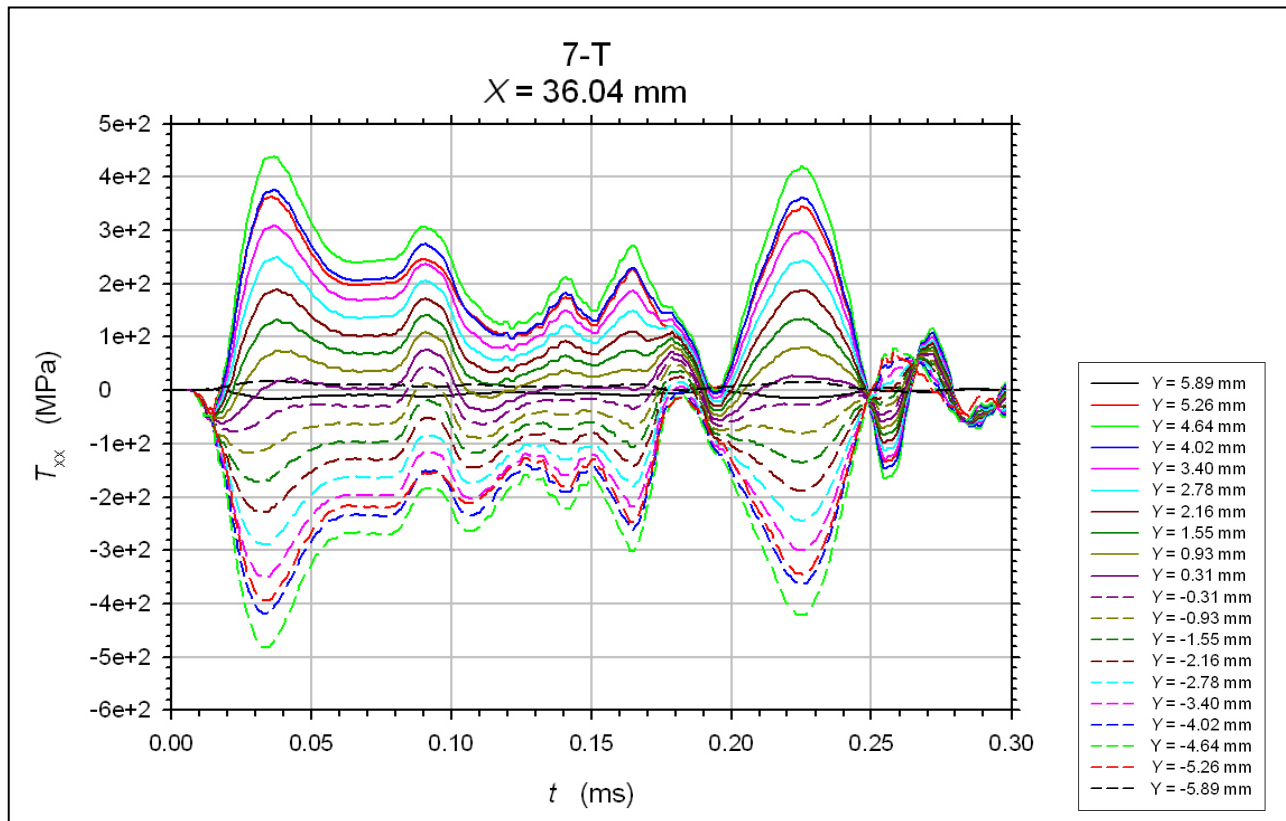


Figure 23.  $T_{xx}$  in rod 7-T along  $X = 36.04$  mm as a function of time after impact. (Note the generally small values of  $T_{xx}$  at  $Y = \pm 5.89$  mm, corresponding to the thread's interior.)

Note that throughout the time range shown, the largest values for  $|T_{xx}|$  occur at  $|Y| = 4.64$  mm, just outside the edge of the central core region. As  $|Y|$  is increased beyond this value,  $|T_{xx}|$  decreases. Thus, figure 23 supports the observation made in section 3.4.4 that the threads in rod 7-T are largely unloaded relative to the central core of the rod.

In appendix B, plane-strain static analyses of rods 7-NT and 7-T, cantilevered at the back end and point loaded at the front, are performed with LS-DYNA in implicit mode. The results for mid-plane deflection are compared with an analytical solution from plate theory. These comparisons further support the picture that the threads of rod 7-T are largely outside the axial load path and decrease the effective thickness of the rod, thereby leading to a larger degree of bending.

### 3.4.6 Profiles of Principal Stresses in Rods 7-NT and 7-T at $X = 35.74$ mm and $t = 32 \mu s$

Bjerke and Edmanson (2004) describe a set of experiments in which a beam composed of 93W-5.6Ni-1.4Fe and with dimensions  $127 \times 9 \times 9$  mm was impacted at the center of its length by a cylindrical projectile of the same material. The projectile had a 44.5-mm length and an 8.9-mm diameter, and the impact speed was 50 m/s (figure 24). The beam split into two pieces in each experiment. Scanning electron microscope (SEM) fractography was performed on the main fracture surfaces. Figure 24 shows an SEM of a fracture surface near its intersection with what

had been the back face of the beam. Signs of planar cleavage are apparent. This suggests the use of a failure criterion based on maximum principal stress.

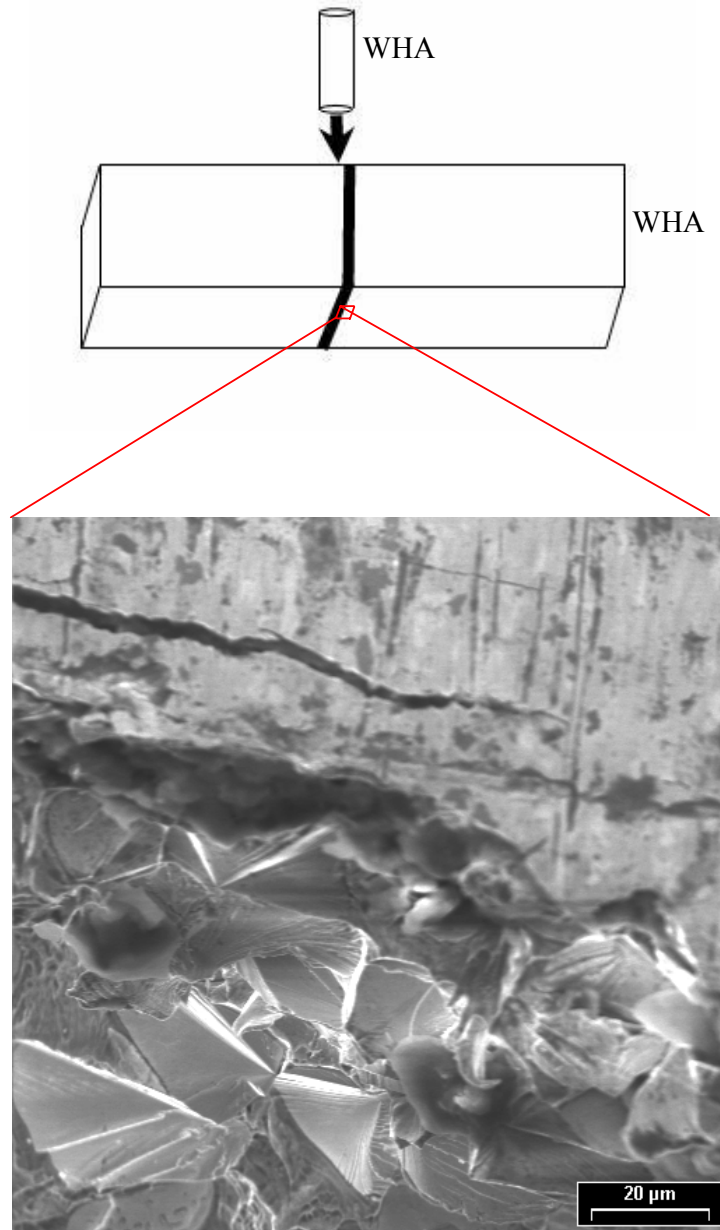


Figure 24. Impact experiment described in Bjerke and Edmanson (2004) and subsequent SEM of fracture surface.

Let  $T_1$ ,  $T_2$ , and  $T_3$  denote the principal stresses, listed in order of increasing magnitude. In plane strain,  $T_2$  is  $T_{zz}$  throughout the rod, and the Mohr's Circle relationships (Fung, 1965, pp. 69-76) can be used to evaluate  $T_1$  and  $T_3$ , as well as the maximum shear stress,  $T_{\text{shear}}$ . We have

$$T_1 = \frac{T_{xx} + T_{yy}}{2} + \sqrt{\left(\frac{T_{xx} - T_{yy}}{2}\right)^2 + T_{xy}^2} \quad (1)$$

$$T_2 = T_{zz} \quad (2)$$

$$T_3 = \frac{T_{xx} + T_{yy}}{2} - \sqrt{\left(\frac{T_{xx} - T_{yy}}{2}\right)^2 + T_{xy}^2} \quad (3)$$

$$T_{\text{shear}} = \sqrt{\left(\frac{T_{xx} - T_{yy}}{2}\right)^2 + T_{xy}^2} \quad (4)$$

The resulting  $Y$ -profiles of the three principal stresses at  $X = 34.74$  mm and  $t = 32 \mu\text{s}$  are presented for rods 7-NT and 7-T in figures 25 and 26, respectively. Profiles of the maximum principal stress,  $T_1$ , and the maximum shear stress,  $T_{\text{shear}}$ , are compared from rods 7-NT and 7-T in figures 27 and 28. Both  $T_1$  and  $|T_{\text{shear}}|$  exhibit larger magnitudes in the vicinity of the threads in rod 7-T than occur anywhere in rod 7-NT. The maximum values computed for  $T_1$  in rods 7-NT and 7-T at  $X = 34.74$  mm and  $t = 32 \mu\text{s}$  are compared in table 3. The maximum observed in 7-T is seen to be 49% larger than that in 7-NT. This suggests a greater likelihood of brittle fracture in rod 7-T than in rod 7-NT even if the fracture threshold stress were the same in the two rods. The greater likelihood of 7-T to fracture would be accentuated if the fracture threshold stress were reduced in the vicinity of the threads by the introduction of flaws during the machining process.

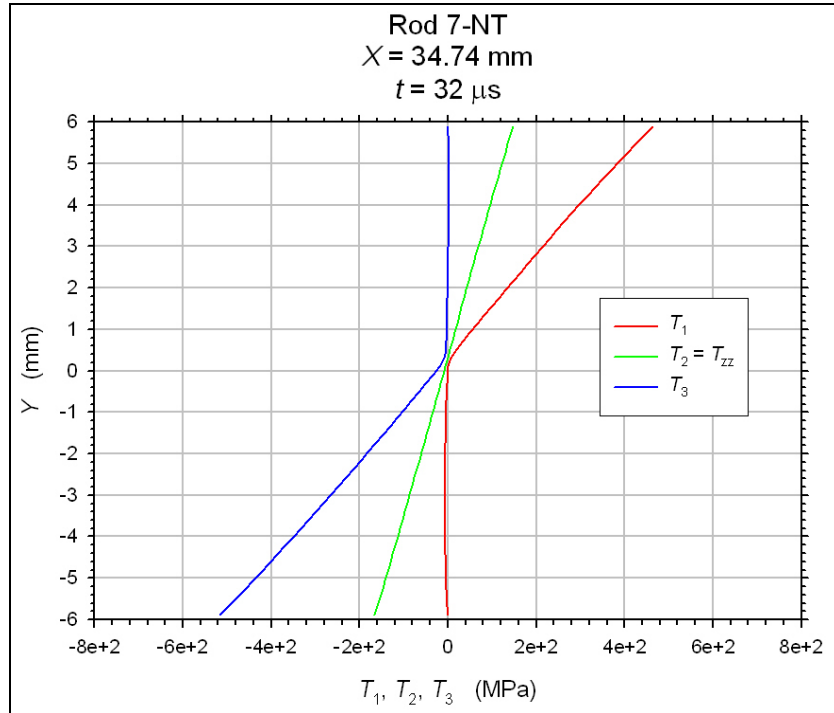


Figure 25. Profiles of principal Cauchy stresses in rod 7-NT along  $X = 34.74$  mm and at  $t = 32 \mu\text{s}$ .

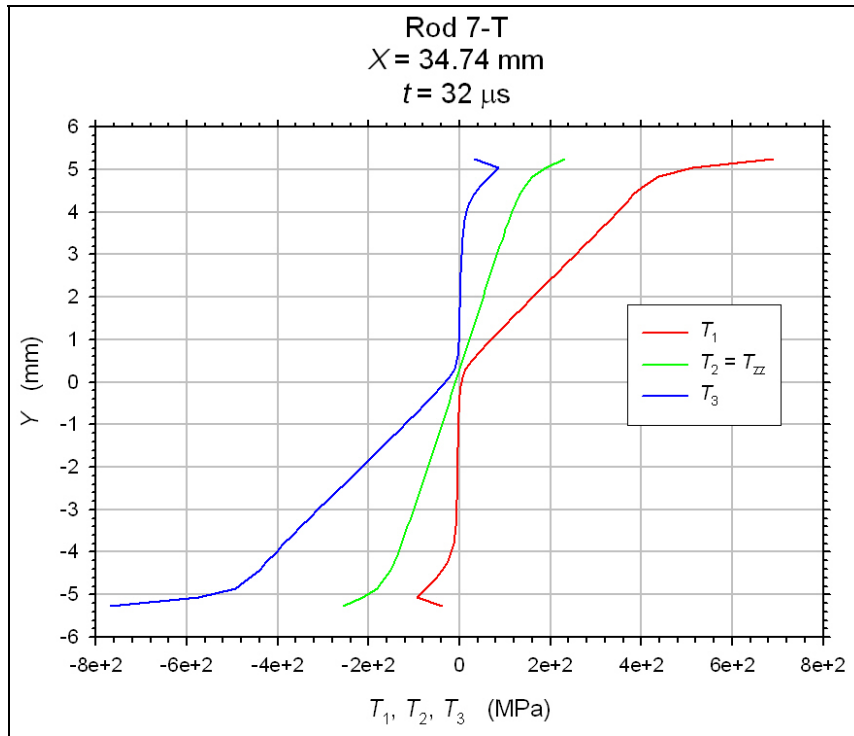


Figure 26. Profiles of principal Cauchy stresses in rod 7-T along  $X = 34.74 \text{ mm}$  and at  $t = 32 \mu\text{s}$ .

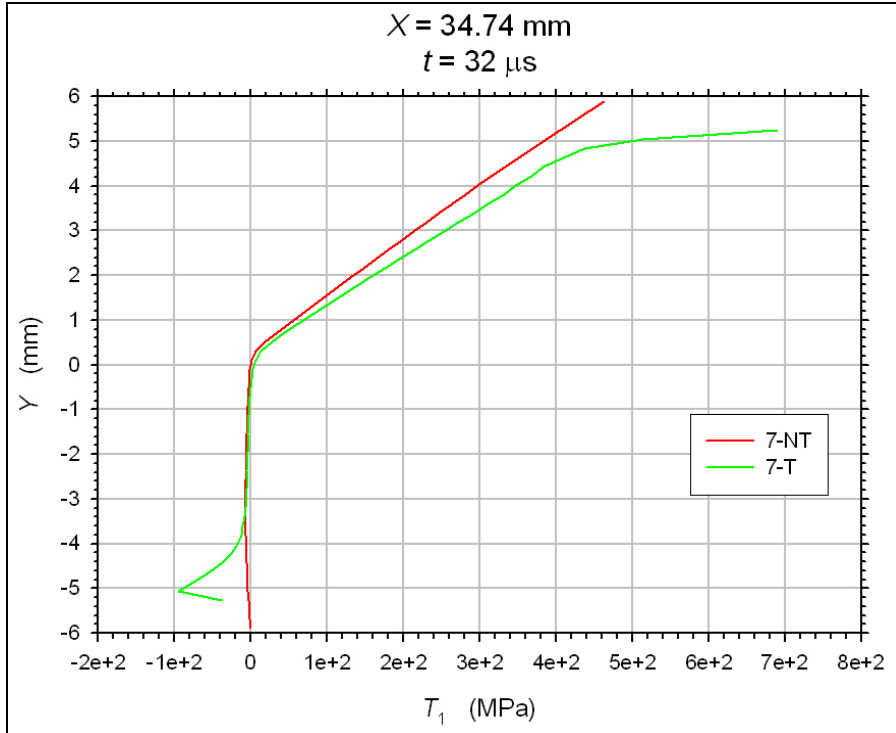


Figure 27. Profiles of maximum principal Cauchy stress in rods 7-NT and 7-T along  $X = 34.74 \text{ mm}$  and at  $t = 32 \mu\text{s}$ .

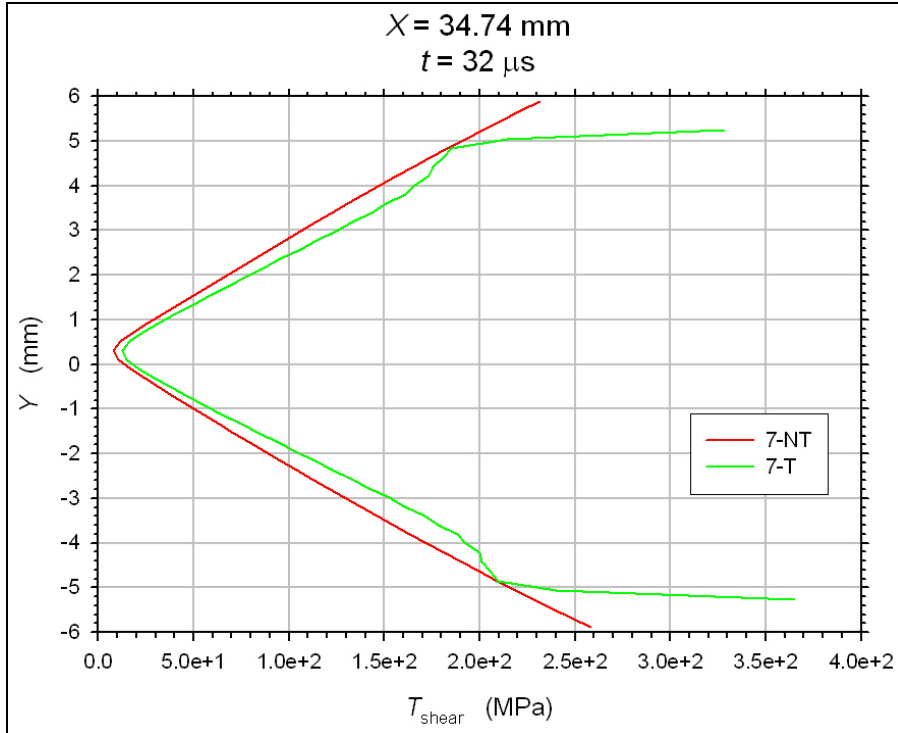


Figure 28. Profiles of maximum Cauchy shear stress in rods 7-NT and 7-T along  $X = 34.74$  mm and at  $t = 32 \mu\text{s}$ .

Table 3. Maximum values of  $T_1$  at  $X = 34.74$  mm and  $t = 32 \mu\text{s}$ .

rod 7-NT		rod 7-T	
max (MPa)	at $Y$ (mm)	max (MPa)	at $Y$ (mm)
463	5.89	690	5.26

---

## 4. Conclusions

---

### 4.1 Summary of Results

In section 2, we presented data from experiments in which small-scale rods composed of 93.1W-4.7Ni-2.2Co WHA were launched into a 9.5-mm-thick RHA plate at 60 degrees' obliquity and a speed of 1300 m/s. Two rod geometries were employed: rod 6A with a 10.2-mm diameter and an  $L/D$  ratio of 16.2, and rod 7 with a 12-mm diameter and an  $L/D$  of 16.7. In ten experiments with threaded rods, five with 6A and five with 7, fracture consistently occurred near the front of the rod. In the four experiments with unthreaded rods, all of rod 7, the results were more varied. In one experiment, fracture did not occur. In another experiment, fracture occurred near the

rod's center. In two other experiments, fracture occurred near the front, as with the threaded rods.

In section 3, we presented FE simulations of the elastic impact of rod 7, both threaded (7-T) and unthreaded (7-NT), upon a rigid surface at a speed of 10 m/s and 60 degrees' obliquity. The LS-DYNA code was used in explicit mode. The impact was found to generate both axial compression waves and flexural waves, with the latter predominant. We focused our post-processing at the distance from the nose of the rod corresponding to the trough between the third and fourth threads in 7-T. We found the axial stress along this cross section to peak at 32  $\mu$ s after initial impact, so we further focused our post-processing on this particular time.

At this cross section and time, rod 7-NT was found to be approximately in a state of pure bending with small superimposed axial compression. The solution in rod 7-T was found to consist of a central core, extending from the center to about 0.8 mm from the base of the threads, in which a state of nearly pure bending plus small axial compression was observed. Outside this central core, the threaded rod displayed a more triaxial state of stress.

Within its central core region, the threaded rod displayed a greater amplitude of bending than did the unthreaded rod at the same distance from the centerline. In appendix B, the source of this enhanced bending in the threaded rod was explored by means of a static analysis of the rods, threaded and unthreaded, point loaded at one end and cantilevered at the other. These static FE analyses were performed with LS-DYNA in implicit mode. The FE solutions were compared with an analytical result from plate theory. The threads were found to have reduced the effective thickness of the rod and to have decreased the rod's flexural rigidity.

Outside the central core region of rod 7-T and thus in the vicinity of the threads, axial stress attained values substantially larger than any observed in 7-NT. Furthermore, a Mohr's circle analysis revealed that the maximum principal stress and the maximum shear stress also attained larger values near the threads of rod 7-T than anywhere in 7-NT. A fracture criterion based on maximum principal stress would therefore predict that the threads cause enhanced susceptibility to fracture under oblique impact.

## **4.2 Assessment**

The FE simulations in this report involved 10-m/s impact upon a rigid surface. The results suggested possible sources for the enhanced tendency of the threaded rod to fracture. The threads reduce the rod's effective thickness and thus its flexural rigidity. The resulting enhanced bending leads to larger axial stresses, which peak near the base of the threads. In addition, the threads resulted in greater triaxiality, particularly in the vicinity of the threads.

Additional possible sources for the enhanced tendency to fracture may be revealed in a 3-D perforation analysis at 1300 m/s. Such an analysis would include out-of-plane modes of deformation, plasticity properties of the WHA, and interactions between the threads and the wall of the penetration channel developed in the RHA.

---

## 5. References

---

Altair Engineering, Inc., [http://www.altair.com/software/hw\\_hm.htm](http://www.altair.com/software/hw_hm.htm), 2005.

Autodesk Corporation, <http://usa.autodesk.com/adsk/servlet>, 2005.

Bjerke, T. W.; Edmanson, W. R. High Rate Deformation and Failure of Tungsten-Sintered Metals. *Proceedings of the 2004 Society for Experimental Mechanics Annual Conference and Exhibition*, Costa Mesa, CA, paper 90, 2004.

Fung, Y. C. *Foundations of Solid Mechanics*, Prentice-Hall: Englewood Cliffs, NJ, pp. 69-76, 1965.

Johnson, G. R. Material Characterization for Warhead Computations, *Tactical Missile Warheads*, editor: J. Carleone, *Progress in Astronautics and Aeronautics*, vol. 55, 1993.

Kolsky, H. *Stress Waves in Solids*, Dover: New York, 1963.

Livermore Software Technology Corporation. *LS-DYNA Keyword User's Manual*. Version 970, Livermore, CA, April 2003.

Timoshenko, S.; Woinowsky-Krieger, S. *Theory of Plates and Shells*, Second Edition, McGraw-Hill: New York, 1959.

INTENTIONALLY LEFT BLANK

---

## Appendix A. Flexural Wave Analysis

---

Kolsky (1963) on pages 48-54 discusses “flexural vibrations of rods.” His “rods” have a finite  $z$ -width, so his analysis must be modified slightly to fit our situation of plates with effectively infinite  $z$ -width (plane strain). In figure A-1, the element of rod between  $x$  and  $x+\Delta x$  is bent into a circular arc with local radius of curvature  $R(x,t)$  at time  $t$ .  $V_y(x,t)$  is the resultant shear force per unit  $z$ -width on face  $x$  at time  $t$ .  $M_z(x,t)$  is the resultant bending moment per unit  $z$ -width on face  $x$  at time  $t$ . Mid-surface deflection  $\delta_y(x,t)$  is defined in terms of the  $y$ -displacement field by

$$\delta_y(x,t) \equiv u_y(x,0,t) \quad (\text{A-1})$$

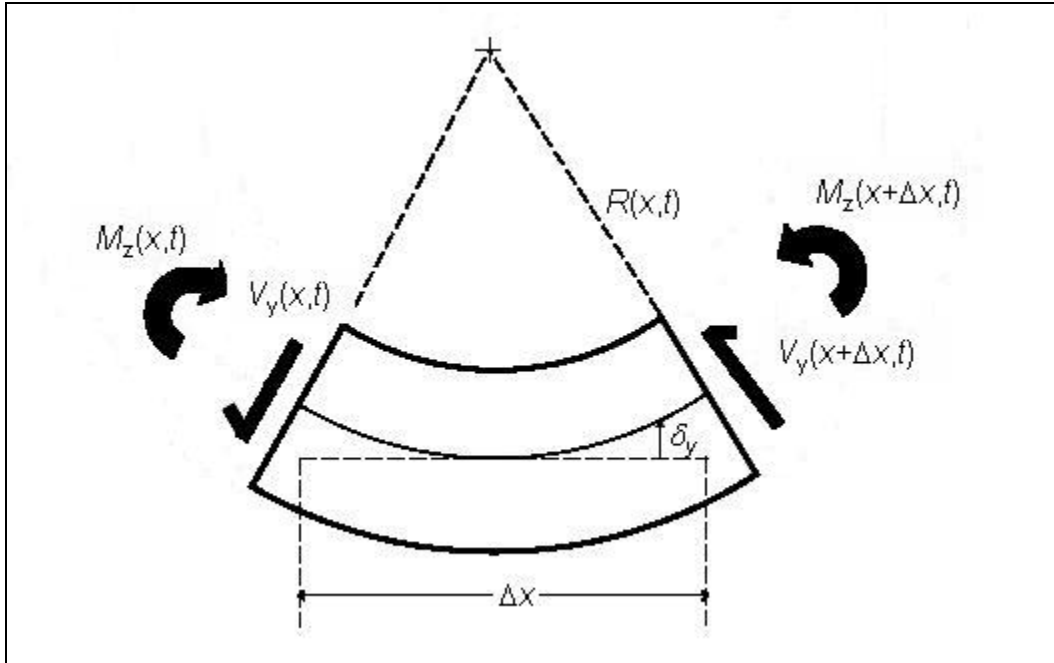


Figure A-1. An element of bent rod at time  $t$ .

The circular arc assumption implies that throughout the rod,

$$e_{xx}(x,y,t) = -\frac{y}{R(x,t)} \equiv -y \frac{\partial^2 \delta(x,t)}{\partial x^2} \quad (\text{A-2})$$

in which  $y$  is distance above the rod's mid-surface.

If we introduce the assumption of plane strain and the approximation  $T_{yy} = 0$ , based on the thinness of the rod, we have

$$T_{xx}(x,y,t) = \frac{E}{1-\nu^2} e_{xx}(x,y,t) = -\frac{Ey}{1-\nu^2} \cdot \frac{\partial^2 \delta_x(x,t)}{\partial x^2} \quad (\text{A-3})$$

The resulting bending moment on face  $x$  per unit  $z$ -width is

$$M_z(x, t) = -\int_{-h/2}^{h/2} y T_{xx}(x, y, t) dy = -\frac{E h^3}{12(1-\nu^2)} \frac{\partial^2 \delta_x(x, t)}{\partial x^2} \quad (\text{A-4})$$

Conservation of  $y$ -momentum applied to the rod element in figure A-1 requires that

$$\rho h \frac{\partial^2 \delta_y}{\partial t^2} = \frac{\partial V_y}{\partial x} \quad (\text{A-5})$$

If we neglect rotary inertia, a reasonable assumption when the wavelength is substantially larger than the rod thickness (Kolsky 1963, pp. 52-53), then conservation of  $z$ -angular momentum requires that

$$V_y = -\frac{\partial M_z}{\partial x} \quad (\text{A-6})$$

so that

$$\frac{\partial^2 \delta_y}{\partial t^2} = \frac{E h^2}{12(1-\nu^2)} \frac{\partial^4 \delta_y}{\partial x^4} \quad (\text{A-7})$$

Consider a traveling wave solution of the form

$$\delta_y(x, t) = \sin[k(x - c_f t)] \quad (\text{A-8})$$

Here,  $c_f$  is the flexural wave speed, and  $k$  is the wave number related to the wavelength  $\lambda$  by

$$k = \frac{2\pi}{\lambda} \quad (\text{A-9})$$

Substitution into equation A-7 yields the characteristic equation

$$k^2 c_f^2 = \frac{E h^2}{12(1-\nu^2)} k^4$$

or

$$c_f = \frac{\sqrt{3}}{6} h k c_0 = \frac{\pi}{\sqrt{3}} \frac{h}{\lambda} \cdot c_0 \quad (\text{A-10})$$

$c_0$  is the axial compression wave speed given by

$$c_0 = \sqrt{\frac{E}{(1-\nu^2)\rho}} \quad (\text{A-11})$$

$c_f < c_0$  whenever

$$\frac{\pi}{\sqrt{3}} \frac{h}{\lambda} < 1$$

or

$$\lambda > \frac{\pi}{\sqrt{3}} h = 1.814 h \quad (\text{A-12})$$

For rod 7-NT,  $h = 12$  mm and  $c_f < c_0$  whenever  $\lambda > 21.77$  mm.

INTENTIONALLY LEFT BLANK

---

## Appendix B. Static Bending of Rods 7-NT and 7-T

---

### B.1 Analytical Solution

In appendix A, we developed equations of motion for the dynamic bending of a plate in plane strain. We now consider the special case of quasi-static bending, so that inertial effects are negligible. Then  $\delta_y$ , deflection of the plate's mid-surface, and  $M_z$ , the resultant bending moment per unit  $z$ -width, can both be treated as functions of  $x$  only. Equation A-4 then becomes

$$\frac{d^2 \delta_y}{dx^2} = -\frac{M_z(x)}{D} \quad (\text{B-1})$$

$D$  is the plate's *flexural rigidity*, a measure of its resistance to bending, and is given by

$$D = \frac{E h^3}{12(1-\nu^2)} \quad (\text{B-2})$$

$E$  and  $\nu$  are Young's modulus and Poisson's ratio, respectively.<sup>4</sup>

Consider the specific boundary conditions shown in figure B-1a. The plate is point loaded at  $x = 0$  and cantilevered at  $x = L$ . The applied load per unit  $z$ -width is  $F$ . The cantilevered boundary conditions are

$$\delta_y(L) = 0 \quad (\text{B-3})$$

$$\frac{d\delta_y}{dx}(L) = 0 \quad (\text{B-4})$$

The rod's free-body diagram and bending moment diagram are shown in figure B-1b and B-1c. The resultant bending moment on the cross section at location  $x$  is

$$M_z(x) = xF \quad ; \quad 0 < x < L \quad (\text{B-5})$$

The substitution of equation B-5 into B-1 and the application of boundary conditions B-3 and B-4 yields the deflection solution

$$\delta_y(x) = -\frac{4(1-\nu^2)F}{E} \cdot \left(\frac{L}{h}\right)^3 \cdot \left[1 - \frac{3}{2}\left(\frac{x}{L}\right) + \frac{1}{2}\left(\frac{x}{L}\right)^3\right] \quad (\text{B-6})$$

---

<sup>4</sup>Equation B-1 is derived in chapter 1 of Timoshenko and Woinowsky-Krieger (1959) as a special case of plate theory, in which the plate's bent configuration involves only one non-zero radius of curvature.

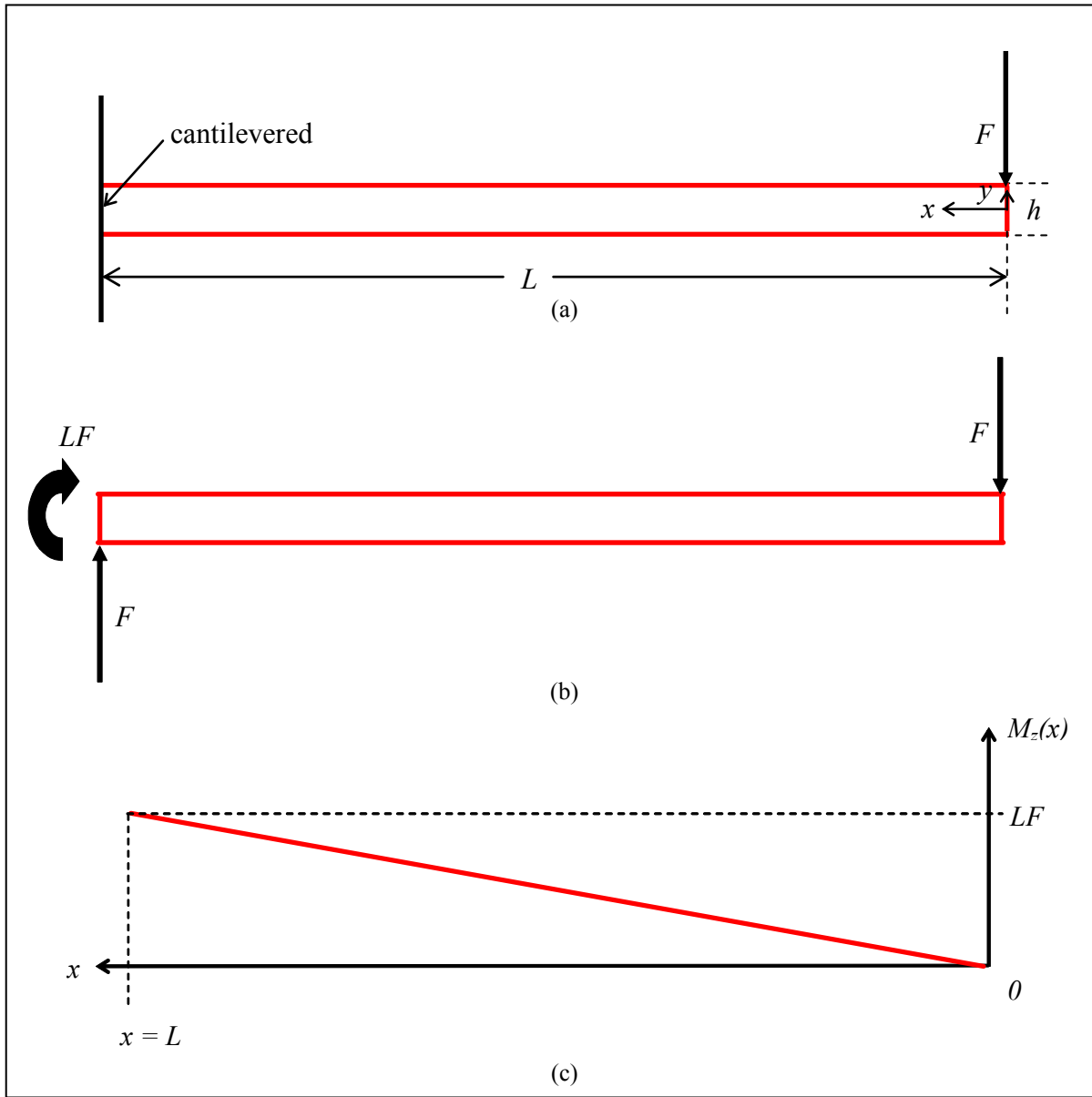


Figure B-1. The quasi-static, plane-strain plate problem studied in section B.1: (a) the plate is cantilevered at one end and point loaded at the other, (b) free-body diagram, (c) bending moment diagram.

Equation B-6 is evaluated in figures B-2 and B-3. Material constants  $E$  and  $\nu$  are assigned the values for WHA in table 1.  $F$  is set to 100 kN/m;  $L$  is set to 200 mm, the length of rods 7-NT and 7-T. Two different values are assigned to thickness  $h$ . In figures B-2 and B-3, we consider  $h = 12$  mm, which is the diameter of the stock of rod 7, as seen in figure 2; 12 mm is therefore the thickness of the entire rod 7-NT and the thickness of rod 7-T based on the peaks of the threads. The other  $h$  value considered in figure B-3 is 10.72 mm. Since each thread has a 0.64-mm dimension (figure 2), 10.72 mm is the thickness of 7-T based on the troughs between the threads.

Figure B-3 shows that an 11% decrease in  $h$  produces a 40% increase in  $\delta_y$  at each  $x$  location. As a consequence of the  $h^3$  dependence of  $D$ , small changes in  $h$  lead to large decreases in bending resistance.

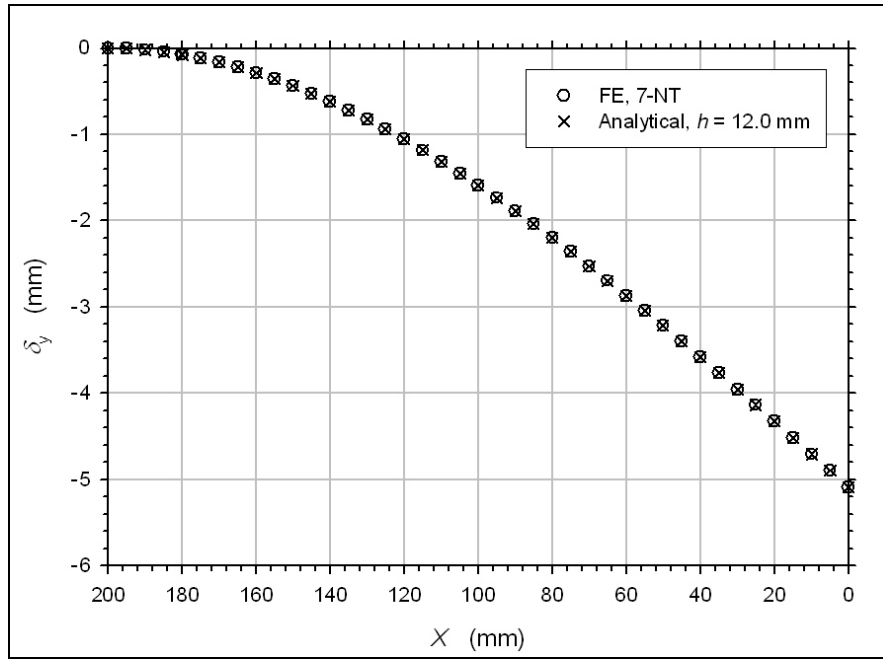


Figure B-2. The mid-plane deflection field computed for rod 7-NT with LS-DYNA closely agrees with the analytical solution for a plate with 12-mm thickness.

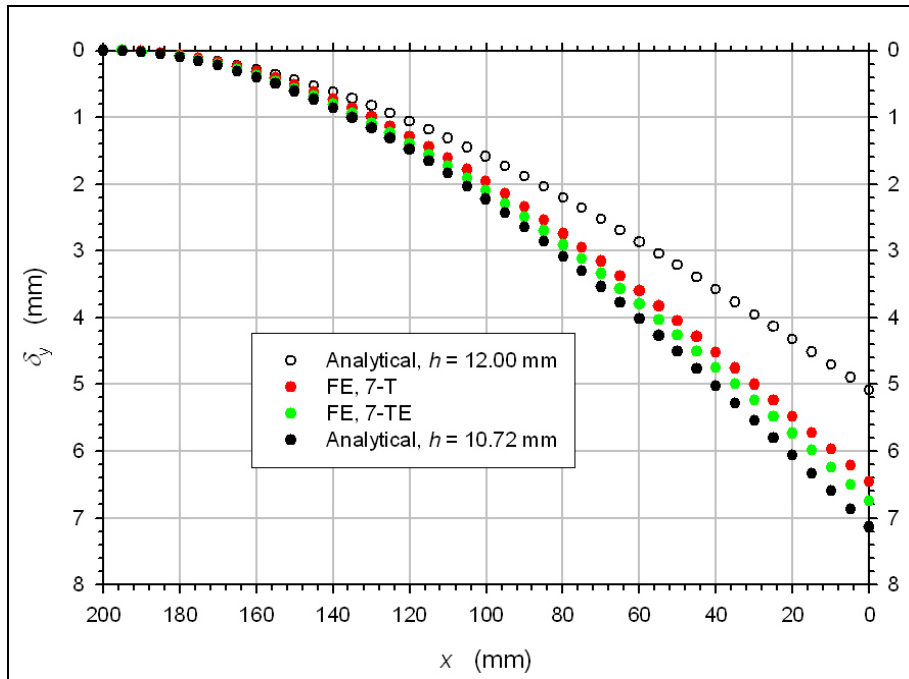


Figure B-3. The mid-plane deflection field computed for rod 7-T with LS-DYNA is bounded by the analytical solution for plates with 12-mm and 10.72-mm thickness and is closer to the latter.

## B.2 FE Solutions for Rods 7-NT and 7-T

Figure B-4 shows rod 7-T point loaded at its front end and cantilevered at its back end. We used LS-DYNA in implicit mode to perform a quasi-static analysis. Force per unit width,  $F$ , was quasi-statically raised to 100 kN/m. This amplitude was chosen so that strains nowhere exceeded 0.005, thus ensuring that the small strain and small displacement approximations were applicable. The meshes in figures 10 and 11 were again used for the two rods. Plane strain (ELFORM=13 on \*SECTION\_SHELL) was again imposed, but in these quasi-static analyses, the two-dimensional elements were fully integrated with four Gaussian quadrature points per element. Material \*MAT\_ORTHOTROPIC\_ELASTIC was again applied in the degenerate isotropic case. The values for  $\rho$ ,  $E$ , and  $\nu$  in table 1 were specified.

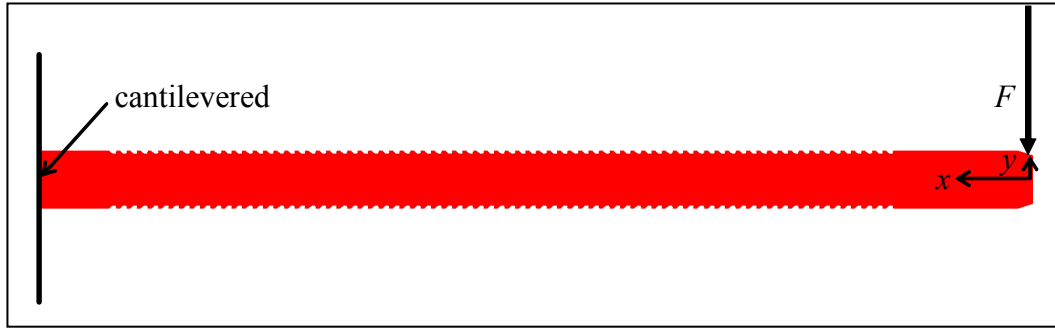


Figure B-4. The quasi-static plane strain problems studied in section B.2: rods 7-NT, 7-T, and 7-TE are each cantilevered at one end and point loaded at the other.

Figure B-2 shows the FE results for  $\delta_y(x)$ , the  $y$ -displacement field of the mid-surface, sampled at 5-mm intervals of  $x$  in rod 7-NT. This FE solution is compared with the analytical solution from plate theory, equation B-6, evaluated with  $h = 12$  mm. The FE solution for rod 7-NT agrees closely with this plate theory solution.

The FE results for  $\delta_y(x)$  in rod 7-T are added to figure B-3. The FE solution is bounded by the plate theory solutions for  $h = 12.00$  and  $10.72$  mm, and is closer to that for  $h = 10.72$  mm. In this sense, the threads have decreased the effective  $h$  of rod 7 with regard to bending.

Rod 7-TE, shown in figure B-5, is created from rod 7-T by the extension of the threaded region into the front and rear of the plate. Threads span 96.8% of the length of 7-TE, as compared with 78.8% of 7-T. LS-DYNA results for 7-TE, point loaded at one end and cantilevered at the other, are added to figure B-3. As expected,  $\delta_y(x)$  results from 7-TE lie between those from 7-T and the analytical solution for  $h = 10.72$  mm.

A plate's effective thickness,  $h_{\text{eff}}$ , can be defined from the analytical solution in equation B-6 as

$$h_{\text{eff}} = L \left[ \frac{4(1-\nu^2)F}{E \delta_y(0)} \right]^{1/3} \quad (\text{B-7})$$

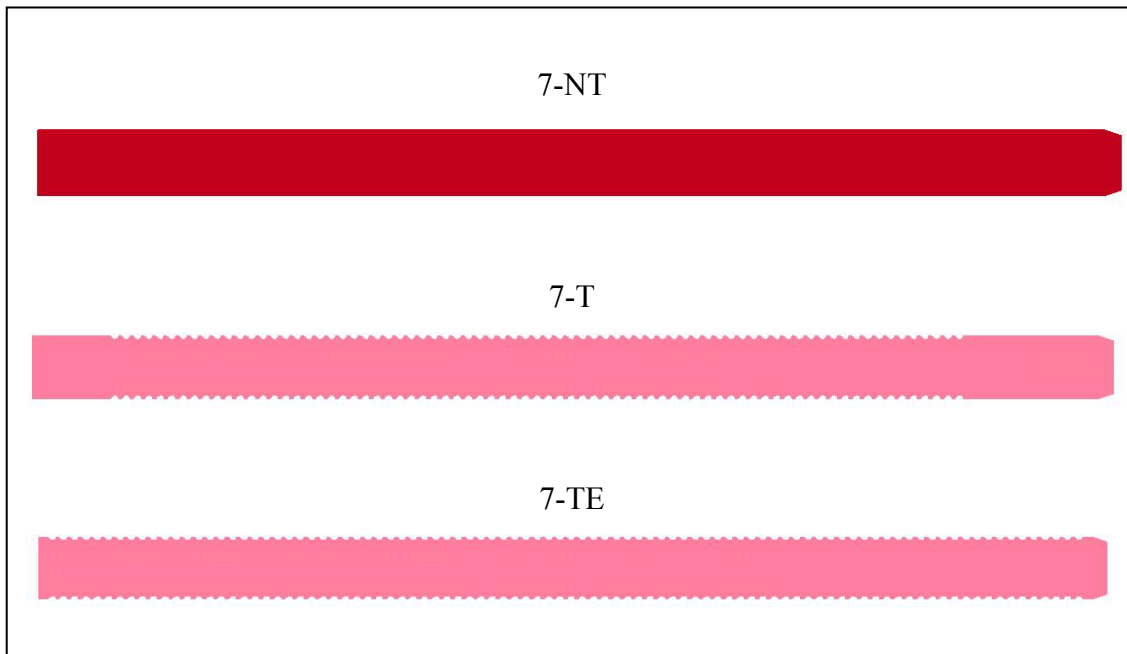


Figure B-5. The profiles of rods 7-NT, 7-T, and 7-TE.

Here,  $\delta_y(0)$  is the midplane deflection at  $x = 0$ . Results for the three plates are compared in table B-1. The effective thickness of rod 7-TE is 0.19 mm larger than the thickness of rod 7 based on the trough between the threads.

Table B-1. Effective thicknesses of the three plates

plate	$\delta_y(0)$ (mm)	$h_{\text{eff}}$ (mm)
rod 7-NT	5.087	11.99
rod 7-T	6.460	11.08
rod 7-TE	6.750	10.91

INTENTIONALLY LEFT BLANK

---

## List of Symbols

---

$D$	flexural rigidity
$E$	Young's modulus
$F$	applied force per unit thickness
$L$	rod length
$M_z$	resultant bending moment per unit $z$ -width
$T_{\text{shear}}$	maximum Cauchy shear stress
$T_{xx}, T_{yy}, T_{zz},$ $T_{xy}, T_{xz}, T_{yz}$	} components of the Cauchy stress tensor
$T_1, T_2, T_3$	
$V_y$	resultant shear force per unit $z$ -width
$X, Y, Z$	material coordinates
$c_0$	speed of axial compression wave
$c_f$	speed of flexural wave
$e_{xx}, e_{yy}, e_{zz},$ $e_{xy}, e_{xz}, e_{yz}$	} components of the infinitesimal strain tensor
$h$	
$h_{\text{eff}}$	plate's effective thickness
$k$	wave number
$t$	time
$u_x, u_y, u_z$	displacement components
$x, y, z$	spatial (laboratory) coordinates
$\delta_y$	$y$ -displacement of the plate's mid-surface
$\lambda$	wavelength
$\nu$	Poisson's ratio
$\rho$	material density

NO. OF  
COPIES ORGANIZATION

- \* ADMINISTRATOR  
DEFENSE TECHNICAL INFO CTR  
ATTN DTIC OCA  
8725 JOHN J KINGMAN RD STE 0944  
FT BELVOIR VA 22060-6218  
\*pdf file only
- 1 DIRECTOR  
US ARMY RSCH LABORATORY  
ATTN IMNE ALC IMS MAIL & REC MGMT  
2800 POWDER MILL RD  
ADELPHI MD 20783-1197
- 1 DIRECTOR  
US ARMY RSCH LABORATORY  
ATTN AMSRD ARL CI OK TL TECH LIB  
2800 POWDER MILL RD  
ADELPHI MD 20783-1197
- 4 DIR ARO  
ATTN A RAJENDRAN A CROWSON  
B LAMATTINA TECH LIB  
PO BOX 12211  
RTP NC 27709-2211
- 4 ARMY HIGH PERFORMANCE  
COMPUTING CTR  
ATTN T HOLMQUIST G JOHNSON  
S BEISSEL R STRYK  
1200 WASHINGTON AVE SOUTH  
MINNEAPOLIS MN 55415
- 1 UNIV OF ALABAMA  
ENGINEERING MECHANICS  
ATTN S E JONES  
PO BOX 870278  
TUSCALOOSA AL 34587-0278
- 1 NORTHWESTERN UNIV  
MECHANICAL ENGINEERING  
ATTN W K LIU  
EVANSTON IL 60208
- 1 NORTHWESTERN UNIV  
CIVIL ENGINEERING  
ATTN T BELYTSCHKO  
EVANSTON IL 60208
- 1 UNIV OF MISSOURI ROLLA  
CIVIL ENGINEERING DEPT  
ATTN W SCHONBERG  
ROLLA MO 65409-0030

NO. OF  
COPIES ORGANIZATION

- 3 JHU MECH ENG  
ATTN K T RAMESH K HEMKER F ZHOU  
LATROBE HALL  
3400 N CHARLES ST  
BALTIMORE MD 21218
- 1 SRI INTERNATL  
ATTN D SHOCKEY  
333 RAVENSWOOD AVE  
MENLO PARK CA 94025-3493
- 1 NORTH CAROLINA STATE UNIV  
DEPT MECH AND AEROSPACE ENG  
ATTN M ZIKRY  
BOX 7910  
RALEIGH NC 27695-7910
- 1 UNIV OF CINCINNATI  
COLLEGE OF ENGINEERING  
ATTN A TABIEI  
787 RHODES HALL  
PO BOX 210070  
CINCINNATI OH 45221-0070
- 2 PURDUE UNIV  
AEROSPACE ENGINEERING  
ATTN W CHEN C T SUN  
315 N GRANT ST  
WEST LAFAYETTE IN 47907-2023
- 1 CALIFORNIA INST OF TECH  
AERONAUTICS AND APPLIED  
MECHANICS  
ATTN M ORTIZ  
PASADENA CA 91125
- 1 DYNA EAST CORP  
ATTN W FLIS  
3620 HORIZON DRIVE  
KING OF PRUSSIA PA 19406-2647
- 2 SOUTHWEST RSCH INST  
ENGR AND MAT SCI DIV  
ATTN C ANDERSON J WALKER  
6220 CULEBRA ROAD  
PO DRAWER 28510  
SAN ANTONIO TX 78228-0510
- 2 UNIV OF TEXAS AT AUSTIN  
INST FOR ADV TECH  
ATTN S BLESS S SATAPATHY  
4030 2 W BRAKER LANE  
AUSTIN TX 78759

NO. OF  
COPIES ORGANIZATION

3 LIVERMORE SOFTWARE TECH CORP  
ATTN J HALLQUIST J DAY M JENSEN  
2876 WAVERLY WAY  
LIVERMORE CA 94550-1740

1 APPLIED RSCH ASSOCIATES  
ATTN D E GRADY  
4300 SAN MATEO BLVD NE  
SUITE A 220  
ALBUQUERQUE NM 87110

4 DIR SANDIA NATL LABS  
ATTN M KIPP E HERTEL  
R BRANNON TECH LIB  
PO BOX 5800  
ALBUQUERQUE NM 87185-5800

1 US ARMY TACOM ARDEC  
ATTN AMSTA AR WEE C E BAKER  
PICATINNY ARSENAL NJ 07806-5000

3 DIR LANL  
ATTN D MANDEL G GRAY  
TECH LIB  
PO BOX 166  
LOS ALAMOS NM 87454

1 INTERNATL RSCH ASSOCIATES  
ATTN D ORPHAL  
4450 BLACK AVE STE E  
PLEASANTON CA 94566-6145

ABERDEEN PROVING GROUND

1 DIRECTOR  
US ARMY RSCH LAB  
ATTN AMSRD ARL CI OK (TECH LIB)  
BLDG 4600

2 DIRECTOR  
US ARMY RSCH LAB  
ATTN AMSRD ARL CI HC A MARK  
R NAMBURU  
BLDG 394

1 DIRECTOR  
US ARMY RSCH LAB  
ATTN AMSRD ARL SL BB D BELY  
BLDG 328

1 DIRECTOR  
US ARMY RSCH LAB  
ATTN AMSRD ARL SL BE R SAUCIER  
BLDG 328

NO. OF  
COPIES ORGANIZATION

4 DIRECTOR  
US ARMY RSCH LAB  
ATTN AMSRD ARL WM J SMITH D LYON  
M FERREN-COKER J MCCAULEY  
BLDG 4600

1 DIRECTOR  
US ARMY RSCH LAB  
ATTN AMSRD ARL WM B T ROSENBERGER  
BLDG 4600

1 DIRECTOR  
US ARMY RSCH LAB  
ATTN AMSRD ARL WM B R COATES  
BLDG 309

1 DIRECTOR  
US ARMY RSCH LAB  
ATTN AMSRD ARL WM BF S WILKERSON  
BLDG 390

1 DIRECTOR  
US ARMY RSCH LAB  
ATTN AMSRD ARL WM M S MCKNIGHT  
BLDG 4600

8 DIRECTOR  
US ARMY RSCH LAB  
ATTN AMSRD ARL WM MB R DOWDING  
D HOPKINS W DEROSSET  
B POWERS M MINNICINO  
J SOUTH J TZENG  
A FRYDMAN  
BLDG 4600

3 DIRECTOR  
US ARMY RSCH LAB  
ATTN AMSRD ARL WM MB M BERMAN  
M CHOWDHURY T H LI  
BLDG 203

10 DIRECTOR  
US ARMY RSCH LAB  
ATTN AMSRD ARL WM MD W ROY  
B CHEESEMAN G GAZONAS  
J LASALVIA E CHIN R DOOLEY  
C FOUNTZOULAS B SCOTT  
S WOLF C F YEN  
BLDG 4600

1 DIRECTOR  
US ARMY RSCH LAB  
ATTN AMSRD ARL WM T B BURNS  
BLDG 309

NO. OF  
COPIES ORGANIZATION

- 4 DIRECTOR  
US ARMY RSCH LAB  
ATTN AMSRD ARL WM TA N GNIAZDOWSKI  
M BURKINS C HOPPEL W GOOCH  
BLDG 393
- 3 DIRECTOR  
US ARMY RSCH LAB  
ATTN AMSRD ARL WM TB P BAKER  
R BITTING R SKAGGS  
BLDG 309
- 25 DIRECTOR  
US ARMY RSCH LAB  
ATTN AMSRD ARL WM TD  
T BJERKE (5 CYS)  
M RAFTENBERG (15 CYS)  
M GREENFIELD S BILYK  
E RAPACKI D CASEM  
J CLAYTON  
BLDG 4600
- 5 DIRECTOR  
US ARMY RSCH LAB  
ATTN AMSRD ARL WM TC  
K KIMSEY L MAGNESS  
D SCHEFFLER S SCHRAML  
W WALTERS  
BLDG 309
- 1 DIRECTOR  
US ARMY RSCH LAB  
ATTN AMSRD ARL WM TE B LOVE  
BLDG 309

NO. OF  
COPIES ORGANIZATION

- 1 P CHANTERET  
INSTITUT SAINT-LOUIS  
MULHOUSE  
FRANCE
- 2 RAFAEL BALLISTICS CTR  
M MAYSELESS ZVI ROSENBERG  
PO BOX 2250  
HAIFA 31021  
ISRAEL
- 1 UNIV OF WATERLOO  
MECHANICAL ENGNRG  
M J WORSWICK  
200 UNIVERSITY AVE  
WEST WATERLOO  
ONTARIO N2L3G1  
CANADA
- 1 ARL ERO  
S SAMPATH  
AERO MECH ENG  
223 MARYLEBONE RD  
LONDON NW1 5TH  
UNITED KINGDOM
- 1 AMC SCI & TECH CTR  
EUROPE  
T J MULKERN  
POSTFACH 81  
55247 MAINZ KASTEL  
GERMANY
- 2 FRAUNHOFER-INSTITUT  
ERNST-MACH-INSTITUT  
V HOHLER E STRASSBURGER  
ECKERSTRASSE 4  
79104 FREIBURG  
GERMANY